JGR Planets

RESEARCH ARTICLE
10.1029/2025JE009148

Controls on Iron-Redox State in Martian Magmas Quantified by Mössbauer Spectroscopy, Colorimetric Wet Chemistry, and XANES Spectroscopy

S. P. Aithala[1], R. A. Lange[2], and M. M. Hirschmann[1]

[1]Department of Earth and Environmental Sciences, University of Minnesota, Minneapolis, MN, USA, [2]Department of Earth and Environmental Sciences, University of Michigan, Ann Arbor, MI, USA

Key Points:

- Analyses of experiments on Fe-rich basaltic glasses inform new expressions that predict Fe-redox speciation in martian magmas
- Quantitative constraints on iron-redox elucidate mass transfer required to explain oxygen fugacity variability on Mars
- A microbeam technique to characterize Fe-redox in martian glasses is introduced to aid future measurements

Supporting Information:

Supporting Information may be found in the online version of this article.

Correspondence to:

S. P. Aithala,
sanath.aithala98@gmail.com

Citation:

Aithala, S. P., Lange, R. A., & Hirschmann, M. M. (2026). Controls on iron-redox state in martian magmas quantified by Mössbauer spectroscopy, colorimetric wet chemistry, and XANES spectroscopy. *Journal of Geophysical Research: Planets*, *131*, e2025JE009148. https://doi.org/10.1029/2025JE009148

Received 14 APR 2025
Accepted 8 FEB 2026

Author Contributions:

Conceptualization: M. M. Hirschmann
Formal analysis: S. P. Aithala, R. A. Lange
Funding acquisition: M. M. Hirschmann
Investigation: S. P. Aithala
Methodology: M. M. Hirschmann
Project administration: M. M. Hirschmann
Supervision: R. A. Lange, M. M. Hirschmann
Visualization: S. P. Aithala
Writing – original draft: S. P. Aithala
Writing – review & editing: R. A. Lange, M. M. Hirschmann

Abstract To elucidate the relationship between oxygen fugacities (f_{O2}) recorded in martian basalts and redox processes in the martian interior, superliquidus 100-kPa furnace experiments on a composition similar to Humphrey (Adirondack basalt) were conducted at variable f_{O2} and temperature. Quenched glasses were analyzed by EPMA, Mössbauer spectroscopy, colorimetric wet chemistry, and microbeam X-ray absorption near edge structure (XANES) spectroscopy. The experiments reveal Mössbauer and wet chemical determinations of silicate glass Fe^{3+}/Fe^{T} agreeing within uncertainty, supporting the accuracy of extended-Voigt-based fitting of Mössbauer spectra when recoil-free fraction is considered. Fe^{3+}/Fe^{T} ratios determined from Mössbauer spectroscopy from Humphrey and previously studied martian-relevant glass compositions are combined to calibrate models that characterize the relationship between Fe^{3+}/Fe^{T}, f_{O2}, temperature, and composition in martian silicate liquids. The models demonstrate, similar to previously investigated silicate liquids, that the correlation between $\log\left(\frac{X_{Fe3+}}{X_{Fe2+}}\right)$ and $\log f_{O2}$ in martian magmas has a slope less than the value (0.25) expected if ferric and ferrous iron oxide mixed ideally. Martian magma Fe^{3+}/Fe^{T} ratios are more temperature-sensitive compared to non-martian compositions, suggesting that temperature variations may contribute to comparatively large f_{O2} variations in martian basalt. The models are applied to demonstrate that the Fe^{3+}/Fe^{T} increases required to explain multiple-log unit changes in f_{O2} in shergottite magma would not increase terrestrial magma f_{O2} as effectively. To aid in future investigations of martian magma redox, a XANES technique that allows for non-destructive, microanalytical characterization of Fe^{3+}/Fe^{T} in natural martian materials and martian-relevant experiments is introduced.

Plain Language Summary The extent to which elements in martian magmas were oxidized or reduced influences the compositions of Mars' crust, mantle, and atmosphere. From rover surveys of Mars's surface and Earth-based investigation of martian meteorites, it is known that magmas generated on Mars span a wider range of oxygen fugacity—an intrinsic parameter that describes the equilibrium redox speciation of multivalent cations—than that observed for typical magmas on Earth. To understand the controls on the oxidation state of martian magmas, we melted a synthetic martian basalt, Humphrey, in a furnace and subjected the melt to variable concentrations of oxygen. The synthetic magmas were rapidly quenched to glass, preserving the atomic bond environments and valences, and analyzed via techniques that quantify the iron oxidation state. Through repeated experiments at different temperatures and oxygen concentrations, we determine the role of temperature, melt composition, and oxygen fugacity on the martian magma iron oxidation state and place quantitative constraints on how changes in the iron oxidation state influences the span of martian magma oxygen fugacity.

1. Introduction

The oxygen fugacity (f_{O2}) of a planet's mantle controls the storage and speciation of redox-sensitive elements throughout planetary reservoirs and thus influences igneous mass transfer processes (i.e., crystallization, partial melting, and degassing; Ballhaus, 1993; Canil, 1997; Carmichael, 1991; Christie et al., 1986; Cottrell et al., 2021; Eugster, 1957; Herd, 2003, 2006, 2019; Herd et al., 2002; Wood, 1990). These processes can alter a planet's capability for habitability, affect the redox and volatile fluxes from planetary interiors (Dasgupta, 2013; Dasgupta & Hirschmann, 2010; Holloway & Jakobsson, 1986; Rohrbach & Schmidt, 2011; Stagno et al., 2013) and influence planetary atmosphere compositions (Hirschmann, 2012; Holland, 2002; Kasting, 1993; Pahlevan et al., 2019; Trail et al., 2011).

On Mars, the f_{O2} recorded by martian magmas, from oxybarometry of igneous rocks, provides constraints on the redox state of the mantle (Barrat et al., 2002; Goodrich et al., 2003; Gross et al., 2013; Herd, 2003, 2006, 2019; Herd et al., 2001, 2002; Howarth et al., 2014; Howarth & Udry, 2017; Jiang & Hsu, 2012; Lin et al., 2005; Lodders, 1998; Nicklas et al., 2021; Peslier et al., 2010; Rubin et al., 2000; Usui et al., 2008; Wadhwa et al., 2001; Walton et al., 2012; Zipfel et al., 2000), as well as redox processes that occur during magmatic ascent and degassing (Balta et al., 2013; Peslier et al., 2010; Righter et al., 2014; Shearer et al., 2013).

Oxybarometry from martian meteorites and Fe^{3+}/Fe^{T} ratios measured on basalts at Gusev crater by the Mössbauer spectrometer on the Spirit rover record f_{O2}s spanning ~7 orders of magnitude, from 4 log units below the quartz-fayalite-magnetite (QFM; O'Neill, 1987) buffer to 3 log units above QFM (Balta et al., 2013; Ferdous et al., 2017; Gross et al., 2013; Herd, 2003, 2006, 2019; Herd et al., 2001, 2002; Nicklas et al., 2021; Peslier et al., 2010; Schmidt et al., 2013; Udry et al., 2020; Wadhwa et al., 2001). This range is greater than the range observed for all but the most extreme and rare Earth basalts and cannot be explained by the plate tectonic processes which are thought to be responsible for much of the redox variability of terrestrial basalt source regions (Carmichael, 1991; Cottrell et al., 2021) owing to Mars' stable lid.

Also unique to martian magmas is the occurrence of individual lithologies for which oxybarometers record early and late crystallization conditions that increase in f_{O2} by up to 4 orders of magnitude (Balta et al., 2015; Castle & Herd, 2017; Gross et al., 2013; Herd, 2019; Peslier et al., 2010). For comparison, terrestrial magmatic f_{O2} evolution during differentiation is typically toward more reducing conditions and rarely more than 1 log unit (Brounce et al., 2017; Cottrell et al., 2021; Helz et al., 2017; Moussallam et al., 2014, 2019a).

The large f_{O2} variations between and within martian lithologies may indicate the operation of mass transfer processes (e.g., changes in Fe^{3+}/Fe^{T} ratios owing to crystallization, degassing, assimilation) which are more effective than those observed in terrestrial lithologies (Brounce et al., 2022; McCubbin et al., 2013; Shearer et al., 2013; Wang et al., 2021). Alternatively, these large f_{O2} variations may indicate that martian magma f_{O2} is more sensitive to mass transfer and temperature variations than terrestrial magmas. If small changes in Fe^{3+}/Fe^{T} of martian magmas translate to greater f_{O2} changes, then modest incorporation of Fe^{3+}-rich material through assimilation (Herd, 2003, 2019; Ostwald et al., 2022) or enrichment in magmatic Fe^{3+} by the preferential crystallization of Fe^{2+} into olivine and pyroxene in unbuffered crystallization scenarios (Castle & Herd, 2017; Peslier et al., 2010) could feasibly account for the wide range of f_{O2} recorded in martian igneous lithologies. We note that martian magmas, typically generated at reducing conditions relative to terrestrial magmas, are expected to shift more in f_{O2} with small changes in Fe^{3+}/Fe^{T} due to the logarithmic relationship between f_{O2} and Fe^{3+}/Fe^{2+} (Kress & Carmichael, 1991). However, the quantitative relationship between oxygen fugacity and Fe^{3+}/Fe^{2+}, as well as large shifts in f_{O2} within oxidized lithologies, are not well established for martian magma compositions.

Better constraints on redox dynamics during igneous processes require a parameterization relating magmatic Fe^{3+}/Fe^{T} to f_{O2}, temperature, composition, and pressure. At present, experimentally benchmarked models describing this relationship (Borisov et al., 2018; Jayasuriya et al., 2004; Kress & Carmichael, 1988, 1991; Sack et al., 1981) are optimized for magmas that are iron- and phosphorous-poor and aluminum-rich relative to martian compositions (Figure 1). Righter et al. (2013) noted the lack of data relevant to martian compositions in these models and presented a provisional model based on experiments on shergottitic compositions. However, this model does not give accurate predictions for Fe^{3+}/Fe^{T} variations found experimentally for a Gusev crater basalt ("Homeplate") (Matzen et al., 2022). We note, that the Homeplate composition investigated by Matzen et al. (2022) was alkali-free owing to concerns of alkali evaporation during their high-temperature experiments, and that the Righter et al. (2013) model predicts that behavior of Fe^{3+}/Fe^{T} in martian magmas is highly sensitive to variations in alkalis. However, the sensitivity of the Righter et al. (2013) model to magmatic alkali contents is unprecedented and requires further investigation to determine if it can accurately predict Fe^{3+}/Fe^{T} across the breadth of compositions relevant to martian magmas.

To provide additional constraints on variations of Fe^{3+}/Fe^{T} as a function of f_{O2} for martian magmas, we conducted experiments on melt compositions representative of Gusev Crater basalt, "Humphrey," (McSween et al., 2006). Glasses of this composition were quenched from a gas-mixing furnace at 100 kPa and a range of f_{O2} and their Fe^{3+}/Fe^{T} ratios characterized by Mössbauer spectroscopy and wet chemical colorimetry. Combining these with data from other martian-relevant compositions (Matzen et al., 2022; Righter et al., 2013) allows calibration of an expression quantifying the effect of f_{O2} on Fe^{3+}/Fe^{T} in diverse martian magmas and thus, investigation of the redox mass transfer processes associated with f_{O2} variations observed in the martian rock record.

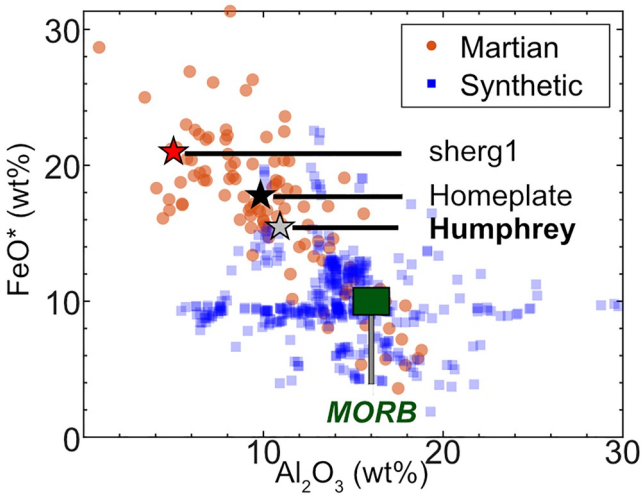

Figure 1. Comparison between martian igneous compositions (orange circles; Filiberto, 2017) and experimentally synthesized silicate liquids investigated to parameterize the relationship between Fe^{3+}/Fe^{T} and f_{O2} (blue squares; Borisov et al., 2018). Star symbols represent martian basalt compositions for which the relationship between Fe^{3+}/Fe^{2+} and f_{O2} has been investigated experimentally (sherg1; Righter et al., 2013, Homeplate; Matzen et al., 2022, Humphrey; originally from McSween et al., 2006, composition modified in present study portrayed above, Table S1). Green rectangle represents the average composition of mid-ocean-ridge basalt.

While this work expands on previous studies investigating martian magma redox, better constraints of iron redox systematics in martian magmas require further characterization of Fe^{3+}/Fe^{T} in martian magmas across a more comprehensive survey of martian compositions (Figure 1). A primary challenge in attaining such data is the application of bulk analytical methods (Mössbauer spectroscopy and wet chemistry), which require large, homogenous glass aliquots. Further, understanding redox mass transfer eventually requires experimental characterization of glasses coexisting with other phases, which would be enabled with a microbeam method of analysis. To facilitate future microbeam Fe^{3+}/Fe^{T} characterization of martian-relevant glasses, we also leverage a subset of experimental to glasses to develop an X-ray absorption near edge structure (XANES) spectroscopic method.

2. Methods

2.1. Sample Preparation

We synthesized a silicate powder with a composition modified from that of Gusev crater basalt Humphrey (McSween et al., 2006) with a slight depletion in FeO* (McSween et al., 2006: 17.89 wt.% FeO*; this study: 15.69 wt.% FeO*), from reagent grade oxides (SiO_2, TiO_2, Al_2O_3, MgO, Fe_2O_3, P_2O_5) and carbonates ($CaCO_3$, Na_2CO_3, K_2CO_3). The Humphrey composition was selected as a typical martian basalt composition (Figure 1) that complements previously investigated FeO*-rich martian compositions (sherg 1, Righter et al., 2013; alkali-free Homeplate, Matzen et al., 2022), while notably being Na_2O-rich (Humphrey: nominally 2.4 wt.%, McSween et al., 2006; sherg1: 1.6 wt%, alkali-free Homplate, 0 wt.%). The synthesized glass is similar to the composition analyzed by the Spirit rover and reported by McSween et al. (2006), but higher in SiO_2 and MgO by 1.5 wt.% and 1.2 wt.% and lower in FeO* by 2.4 wt.% (Table S1). To enhance the Mössbauer signal, 10% of the Fe_2O_3 was added as pure $^{57}Fe_2O_3$ (Isoflex). Despite concerns of time- and temperature-dependent volatile loss in 100-kPa furnace experiments (Corrigan & Gibb, 1979; Matzen et al., 2022; Tsuchiyama et al., 1981), we included sodium, potassium, and phosphorous, as they influence Fe^{3+}/Fe^{T} – f_{O2} relations (Borisov et al., 2013, 2015, 2017, 2018; Jayasuriya et al., 2004; Righter et al., 2013). The parental magma of the Humphrey composition contains S (3200 ppmw; McSween et al., 2006). However, we excluded sulfur to avoid potential post-quench Fe-S redox exchange during wet chemical analysis (Bézos et al., 2021; Bézos & Humler, 2005; Christie et al., 1986).

Before weighing, SiO_2, TiO_2, Al_2O_3 and MgO were dried for 24 hr at 1000°C, Fe_2O_3 was dried at 800°C for 1 hr, and the carbonates were dried at 400°C for 24 hr. Apart from Fe_2O_3 and P_2O_5, all oxides and carbonates were weighed, combined in an agate mortar and pestle, and homogenized by grinding under ethanol for more than 2 hr. The homogenized mixture was decarbonated by heating from 400 to 1000°C at a rate of 100°C/h, reweighed, and then added to an agate mortar and pestle with the Fe_2O_3-$^{57}Fe_2O_3$ mixture and P_2O_5, added as diammonium phosphate ($(NH_4)_2HPO_4$). The resulting mixture was ground under ethanol for more than 2 hr and then split into two batches: an unmodified, oxidized mixture (100% Fe as Fe_2O_3) and a reduced mixture, annealed in a horizontal gas-mixing furnace set to ~QFM-2 at 1000°C for 24 hr, reducing most of the Fe_2O_3 to FeO.

2.2. 100 kPa Experiments

We heated Humphrey to superliquidus temperatures in a Deltech DT-28-VT-HN-C vertical furnace with a CO/CO_2 or CO_2/O_2 gas mix for f_{O2} control. Temperature was monitored by either a Type B ($Pt_{94}Rh_6$—$Pt_{70}Rh_{30}$) or Type S (Pt—$Pt_{90}Rh_{10}$) thermocouple, calibrated against the nominal melting temperature of gold (Type B = 1060°C, Type S = 1062°C, nominal = 1064°C). The f_{O2} of the experiments was monitored by a SIRO2 C700+ Solid Zirconia Electrolyte oxygen sensor calibrated against the Ni-NiO buffer (Huebner & Sato, 1970).

Experimental charges comprised ~30–35 mg of Humphrey bonded to Pt, Pt-Fe alloy, or Re wire loops using hydrated polyvinyl alcohol (PVA). The choice of metal was f_{O2}-dependent to minimize Re dissolving in the melt under oxidizing conditions, and iron alloying with platinum under reduced conditions. At intermediate f_{O2} where Fe loss to Pt and Re dissolution in melt is significant ($-9 < \log f_{O2} < -4.5$ at 1365°C), we utilized Pt-Fe loops

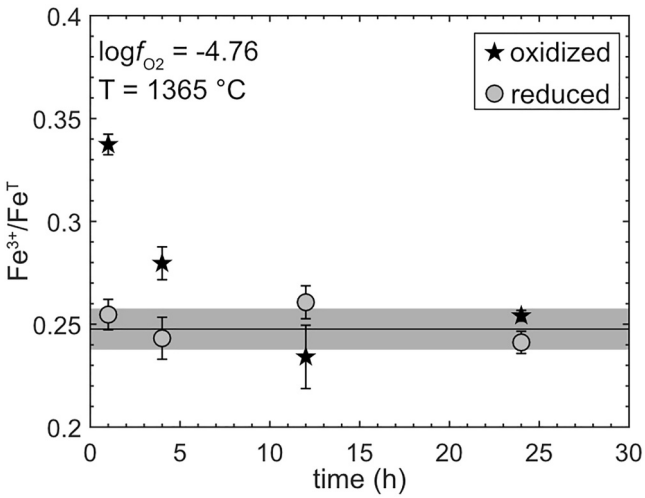

Figure 2. Mössbauer-determined Fe^{3+}/Fe^{T} ratios for time series experiments (1, 4, 12, and 24 hr) conducted at log $f_{O2} = -4.76$ at 1365°C using oxidized ($Fe^{3+}/Fe^{T} = 1$; black stars) and reduced ($Fe^{3+}/Fe^{T} \sim 0.1$; gray circles) splits of the Humphrey starting mix. Solid black line and gray field represent inferred equilibrium value of $Fe^{3+}/Fe^{T} = 0.248 \pm 0.010$. All error bars represent 2-σ uncertainties for Fe^{3+}/Fe^{T} ratios.

with Fe concentrations that mitigate interdiffusion of Fe between melt and alloy. The Pt-Fe alloy loops were fabricated by holding Humphrey-Pt experimental charges to ~1365°C and the target f_{O2} for more than 6 hr, achieving equilibrium interdiffusion of Fe between melt and alloy by the reaction:

$$Fe_{alloy} + \frac{1}{2}O_2 \leftrightarrow FeO_{melt} \quad (1)$$

The experimental charge was then quenched, and the resulting glass was cleaned from the loop using dilute HF_{acid}, producing Pt-Fe wires with optimized Fe concentrations to minimize Fe loss from the melt at intermediate f_{O2}s. Experiments were terminated by dropping the charges into deionized water at 293 K. The resulting glassy beads were sectioned with a tungsten wire saw, producing multiple chips for various analytical procedures.

2.2.1. Time Series

To ensure that Humphrey reached redox equilibrium with minimal time-dependent volatile loss, we conducted time series experiments by holding oxidized and reduced Humphrey mixes at ~1365°C at log $f_{O2} = -4.76$ for 1, 4, 12, and 24 hr and quantifying their Fe^{3+}/Fe^{T} by Mössbauer spectroscopy at 293 K (Figure 2). The Fe^{3+}/Fe^{T} of the oxidized and reduced starting mixes both converged to the same ratio (0.248 ± 0.010), but the reduced starting mix did so more rapidly (<4 hr compared to 24 hr for the oxidized mix). Consequently, all equilibration experiments at 1365°C were conducted between 6 and 24 hr using the reduced starting mix.

2.2.2. f_{O2} Series

To constrain Fe^{3+}/Fe^{T} variation for Humphrey as a function of f_{O2}, we conducted superliquidus equilibration experiments at 100 kPa and 1365°C at log $fO2 = -11.18$ to -0.20. Given the logarithmic relationship between Fe^{3+}/Fe^{T} and log f_{O2}, we ensured that experiments conducted between log $f_{O2} = -8.7$ –> -4.2 were no more than 1 log unit apart to capture significant changes in Fe^{3+}/Fe^{T} for small increments in log f_{O2} (Borisov et al., 2018; Fudali, 1965; Kress & Carmichael, 1991; Matzen et al., 2022; Righter et al., 2013; Sack et al., 1981).

2.2.3. Temperature Series

The effect of temperature on the Fe^{3+}/Fe^{T} ratio of Humphrey was investigated in experiments conducted in air spanning 1250–1500°C. This temperature interval is the span between the approximate liquidus of Humphrey and the upper limit of the vertical-furnace apparatus. To mitigate volatile loss, experiment durations decreased with increasing temperature: 72 hr for 1250°C, 24 hr for 1300°C, 6 hr for 1365°C and 1400°C, 2 hr for 1450°C, and 1 hr for 1500°C.

2.3. Electron Microprobe

Textures of experimentally synthesized glasses were characterized by back-scattered electron and secondary electron imaging, and chemical homogeneity was validated by wavelength dispersive spectroscopy (WDS) using the JEOL JXA-8530F + Electron Probe Microanalyzer at the University of Minnesota. WDS analyses were conducted at 15 kV acceleration voltage with a 10 μm diameter beam of 20 nA. Counting times were 20 s per point for unknowns and 10 s per point for standards. The standards utilized were Springwater olivine for Mg and Si, Kakanui hornblende for Ti, Na, K, almandine garnet for Al, pyrope for Fe, and Durango fluorapatite for Ca and P. The primary standards were selected based on their accuracy in reproducing reference compositions of basaltic glass standards TB-1G (Potts et al., 2002), K411, K412 (Marinenko, 1982), and BCR2-G (Jochum et al., 2006). Primary and secondary standards were analyzed with 5 and >11 unique spots, respectively. All matrix corrections were calculated in the Probe for EPMA software (Donovan & Tingle, 1996).

2.4. Mössbauer Spectroscopy

Mössbauer spectroscopy was conducted in constant acceleration mode with a velocity range of ±12 mm/s with the SEE Co. MS6 spectrometer at 293 K at the Institute for Rock Magnetism, University of Minnesota. A ^{57}Co/Rh source and Reuter Stokes proportional Ar gas counter were employed. Data were collected over 512 channels and then folded to produce 256 unique channels. Calibration was relative to a 25 μm thick α-Fe foil measured at 293 K. We prepared samples by crushing <11 mg to fine sand texture, mixing it with Spectroblend (Chemplex Industries), and packing it into 12.7 mm diameter Delrin cups (Mössbauer thickness <0.15 mg ^{57}Fe/cm^2) for analysis. Data were collected for a minimum of one day and all spectra included 700,000 counts per channel.

All 293-K energy-domain Mössbauer spectra were fitted using extended Voigt based fitting (xVBF) methods computed in the RECOIL software package (Lagarec & Rancourt, 1997). Sextets were not observed in the spectra, indicating that all Fe is paramagnetic Fe^{2+} and Fe^{3+}. The relative contributions of Fe^{2+} and Fe^{3+} in the spectra were determined using 2-D quadrupole doublets with unconstrained CS and QS. For line-broadened, asymmetric Mössbauer spectra observed in amorphous silicate glasses, Fe^{2+} doublets were modeled as asymmetric doublets by correlating CS to QS and allowing δ_{CS} and δ_{QS} to vary (Alberto et al., 1996). To optimize fitting based on the glass f_{O2} and expected contributions to the total spectra, we used three distinct fitting protocols to fit Fe^{3+}.

1. For glasses synthesized at $\log f_{O2} < -7$, Fe^{3+} was fit using a symmetric doublet where CS and QS were allowed to vary, but the δ_{CS} was set to 0 and δ_{QS} was constrained to 0.4. Zhang et al. (2015) adopted this approach to fit Mössbauer spectra for glasses synthesized at reduced conditions where the contribution of paramagnetic Fe^{3+} is less distinguishable in the total spectra, as allowing δ_{QS} to vary freely leads to the doublet collapsing into a non-physical line shape.
2. For glasses synthesized at $-7 < \log f_{O2} < -5$, we treat the contribution of Fe^{3+} as a symmetric doublet where δ_{CS} is set to 0 and δ_{QS} is unconstrained.
3. For glasses synthesized at $\log f_{O2} < -5$, Fe^{3+} is fit as an asymmetric doublet with correlated CS and QS.

This approach of fitting Fe^{3+} is optimal for calculating physically accurate lineshapes at reduced conditions, capturing the real asymmetry of the Fe^{3+} doublet at oxidized conditions, while avoiding overfitting at intermediate f_{O2}. Fe^{3+}/Fe^{T} was calculated from the area ratios of the Fe^{3+} and Fe^{2+} doublets, corrected by the ratio of Lamb-Mössbauer factors of Fe^{3+} and Fe^{2+}, in multicomponent silicate glasses at room temperature as determined by Roskosz et al. (2022; $C = 1.203 \pm 0.033$). The uncertainties were calculated using Bootstrap Aggregration in the RECOIL software package (Lagarec & Rancourt, 1997), which quantifies the uncertainty between the spectra and the lineshapes used to fit them.

2.5. Colorimetric Wet Chemical Ferrous Iron Analyses

The colorimetric method of Wilson (1960) was used to quantify the concentration of ferrous iron (as wt.% FeO) for a subset of the experimental glasses across six separate analytical sessions. Each glass sample was weighed on a microbalance and transferred to a 2 oz. Teflon bottle where it was digested at 293 K in a solution comprising 1.0 mL each of ammonium metavanadate and hydrofluoric acid. The introduction of the ammonium metavanadate solution quantitatively converts Fe^{2+} during digestion to equal moles of V^{4+} following the reaction:

$$V^{5+} + Fe^{2+} \leftrightarrow V^{4+} + Fe^{3+}, \quad (2)$$

which proceeds to completion in acidic solutions.

To recover Fe^{2+} following dissolution, the solution was mixed with 10 mL of ammonium acetate solution, basifying the combined solution and converting all V^{4+} back to the original Fe^{2+} in the sample. We then added to the solution 5 mLs of a coloring reagent (2-2′ bipyridine), which complexes with Fe^{2+}. The contents of each bottle were transferred to 100-mL flasks and diluted with distilled water to the 100-mL mark. The optical density of the solution in each flask was measured at 525 nm in a 1-cm cell using a Perkin-Elmer double-beam spectrophotometer. The optical density was then converted into milligrams of FeO by comparison to the optical densities of standard solutions (made with ferrous ammonium sulfate) containing 0, 50, 200, 400, 500, 600 and 800 mg of FeO (Wilson, 1960; Data set S1). The wt.% FeO in each sample was calculated from the mg of FeO analyzed with the spectrophometer divided by the total weight of glass sample digested in each Teflon bottle.

We calculated wt.% Fe_2O_3 and Fe^{3+}/Fe^T by the difference: Fe_2O_3 (wt.%) = 1.1113(FeO*(wt.%) – FeO(wt.%)), where FeO* (wt.%) was determined via EPMA. To ensure that the wet chemical colorimetric procedure characterized FeO concentrations accurately, we also analyzed two standards certified for analysis of wt.% FeO: Canadian Geological Survey standard SY-4 (Bowman, 1995) and U.S. Geological Survey standard W-2a (Flanagan & Kirschenbaum, 1984), and verified that the average wt.% FeO analysis for the two standards (2.83 ± 0.10; 8.29 ± 0.14 wt.% FeO. 1 − σ) reproduces certified values (2.86 and 8.34 wt% FeO, respectively). We calculated the uncertainties of Humphrey glass measurements by calculating the standard deviation of Fe^{3+}/Fe^T ratios obtained from replicate analyses of a single experimental run product.

2.6. X-Ray Absorption Near-Edge Structure (XANES) Spectroscopy

Fe K-edge XANES spectra were collected on Humphrey experimental glass and basaltic glass standards (Cottrell et al., 2009) in 2 sessions at beamline 13-IDE at the Advanced Photon Source, Argonne National Laboratory and two sessions at beamline 4-BM at the National Synchrotron Light Source II, Brookhaven National Laboratory. At least 5 spectra were collected from distinct spots on each glass, with spot size on all samples set to 10 × 10 or 20 × 20 μm, and incident flux rates set between 1 and 3×10^{10} photons/s to manage detector saturation and limit oxidative beam-damage (Cottrell et al., 2018). Energy selection was achieved using a fixed exit, liquid nitrogen cooled double crystal monochromator and a Si (311) crystal set. X-ray fluorescence from the samples were detected by a Vortex ME4 silicon-drift diode array detector array coupled to a high-speed digital spectrometer system (Quantum Xpress3). Data collected were corrected for detector dead time.

Spectra were recorded from 7012 to 7350 eV in three regions: 2.5 eV steps from 7012 to 7102 eV; 0.1 eV steps from 7102 to 7120 eV, prioritizing the pre-edge; 1.0 eV steps from 7120 eV to 7350 eV. Dwell times for scans were initially set to 2 s per step but optimized to 1 s after determining there was no compromise in spectrum quality. Beam damage time-series analyses, involving irradiation of a single spot of our experimental glass for 300 s and monitoring its absorption intensity at 7113.300 eV, showed no significant increase in absorption intensity over time, indicating negligible oxidative beam damage, as expected in anhydrous mafic glasses (Cottrell et al., 2018).

The shape of the Fe K-edge absorption spectra, determined by the energies and intensities of the Fe-Ka pre-edge (1s-3d) and the main absorption edge (1s-4p) are sensitive to the bonding environment and coordination of Fe in materials (Bajt et al., 1994; Berry et al., 2003; Cottrell et al., 2009; Dyar et al., 2023; Wilke et al., 2001) and have been shown to vary smoothly with changes in iron oxidation state for glasses (Berry et al., 2018; Cottrell et al., 2009; Wilke et al., 2001; Zhang et al., 2018). We quantified the pre-edge centroid energy as a proxy for shape-variation in the Humphrey glasses and basaltic glass standards synthesized by Cottrell et al. (2009) and multiplicatively normalize their values to the established pre-edge centroid energy of standard glass, LW_0 ≡ 7112.3 eV (Cottrell et al., 2009), to allow for comparison of the pre-edge energies across analytical sessions.

Data were processed using the Larch XAS analysis package (Newville, 2013). All spectra were edge-step normalized by fitting a constant line to a subset of the EXAFS region (7200–7350 eV) and setting it to 1. The pre-edge region was modeled as a linear combination of a linear + Lorentzian baseline with two Gaussian subpeaks from 7105 to 7118 eV, and pre-edge centroid energies were extracted by calculating the area-weighted centroid position of the baseline-subtracted pre-edge region.

3. Results

3.1. Major Element Composition and Textures

EMPA analyses of the secondary glass standards reproduce all oxide components within 0.26 wt.% absolute (Table S1). In particular, measurements of FeO*, whose accurate determination is needed for determining Fe^{3+}/Fe^T through wet chemical techniques, are reproduced within 0.20 wt.% absolute and 2.02% relative. Time dependent loss of Na_2O and P_2O_5 were observed in the time series experiments (Na_2O: ∼3.12–2.56 wt. % and P_2O_5: ∼0.55–0.38 wt. % from 1 to 24 hr). Compositional variation from loss of alkalis and phosphorous may affect glass Fe^{3+}/Fe^T, but this effect is expected to be small owing to the small absolute abundance of these species.

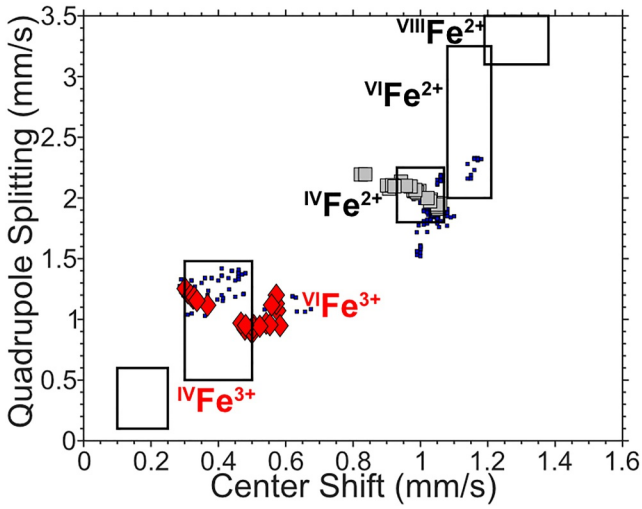

Figure 3. Comparison of center shift and quadrupole splitting values from fitted Fe^{2+} and Fe^{3+} doublets to Mössbauer spectra of Humphrey glasses (gray and red symbols; $n = 25$). Rectangular fields represent typical ranges of hyperfine parameters of $^{IV}Fe^{3+}$, $^{VI}Fe^{3+}$, $^{IV}Fe^{2+}$, $^{VI}Fe^{2+}$, and $^{VIII}Fe^{2+}$ in Fe-bearing solids and are redrawn from Dyar et al. (2006). The small blue squares are the hyperfine parameters for Fe^{2+} and Fe^{3+} doublets from 293 K Mössbauer analyses of basaltic and andesitic glasses from Jayasuriya et al. (2004), Cottrell et al. (2009) with fit parameters are from Zhang et al., 2018), Borisov and McCammon (2010), Righter et al. (2013), Zhang et al. (2016), and Matzen et al. (2022) ($n = 114$).

No crystalline features are evident from BSE images in any of the experimental glass run products, except for experiment VF271 (low end of temperature series: 1250°C), indicating that all other experiments achieved complete melting and rapid quenching to glass. VF271 included a small percentage of olivine crystals, believed to have precipitated during the experiment, and otherwise consisted of homogeneous glass. Average compositions for all experiments containing 100% modified-Humphrey glass ($n = 26$) are cataloged in Table S1 while compositional data for each experimental glass can be found in Data set S1 in the Supporting Information.

3.2. Determination of Fe^{3+}/Fe^{T} Ratio

3.2.1. Mossbauer Spectroscopy

The chi-square goodness-of-fit and hyperfine parameters of these fits are found in Table S2. The hyperfine parameters of all Mössbauer fits are consistent with the hyperfine parameters expected for Fe^{2+} and Fe^{3+} in Fe-bearing solids (Dyar et al., 2006; Figure 3).

For the isothermal series (Table 1), Mössbauer determined Fe^{3+}/Fe^{T} ratios increase as a function of f_{O2}, with $\log\left(\frac{X_{Fe3+}}{X_{Fe2+}}\right)$ versus $\log f_{O2}$ demonstrating a broadly linear relationship, with weighted-least-squares regression yielding a slope of 0.1928 (Figure 4) (1-σ = 0.0108, $R^2 = 0.941$). This linear relationship breaks down for the most reducing experiment VF257 synthesized at $\log f_{O2} = -11.18$, which has greater Fe^{3+} than expected from the otherwise linear trend. To determine if the $\log\left(\frac{X_{Fe3+}}{X_{Fe2+}}\right)$ for VF257 was an outlier, we conducted another linear regression where the datum was removed and compared how the slope of $\log\left(\frac{X_{Fe3+}}{X_{Fe2+}}\right)$ versus $\log f_{O2}$ changed. The regression obtained for this subset of data was not significantly different from the regression obtained previously (with VF257 removed: slope = 0.1979, 1-σ = 0.0105, $R^2 = 0.951$; Figure 4). Therefore, we do not believe that VF257 is an outlier and include it in all future regressions and interpretations.

Mössbauer-determined Fe^{3+}/Fe^{T} ratios for temperature series glasses conducted in air ($\log f_{O2} \equiv -0.68$) from 1300 to 1500°C demonstrate a decrease in Fe^{3+}/Fe^{T} with increasing temperature, with a weighted-least-squares regression of $\log\left(\frac{X_{Fe3+}}{X_{Fe2+}}\right)$ versus the inverse of temperature (K^{-1}) having a positive, linear correlation (slope = 2785, 1-σ = 241.8, $R^2 = 0.976$; Figure 5). The 1250°C experiment (VF271) was not analyzed by Mössbauer spectroscopy as bulk analysis of the partially crystallized experiment would yield a spectrum influenced by Fe-nuclei in both glass and crystalline portions. The Fe^{3+}/Fe^{T} ratio of the VF271 glass is estimated using XANES in Section 4.8.2 and is shown in Figure 5 but not considered in the linear regression owing to its compositional differences from the 1300–1500°C experiments.

3.2.2. Wet Chemical Colorimetry

Glass FeO contents are recorded in Table 2 and the sample masses, absorbances, and calibration curves are in the supplement (Data set S1). The average and standard deviation in wt.% FeO are calculated from FeO determination between duplicate and triplicate measurements, which are then propagated to estimate uncertainties in Fe^{3+}/Fe^{T}.

Similar to the Mössbauer-determined Fe^{3+}/Fe^{T} ratios, wet chemical determinations of Fe^{3+}/Fe^{T} increase as a function of f_{O2}, and weighted-least-squares regression of $\log\left(\frac{X_{Fe3+}}{X_{Fe2+}}\right)$ versus $\log f_{O2}$ trends linearly (slope = 0.1954; $1 - \sigma = 0.0084$, $R^2 = 0.912$), albeit with a larger spread apparent in the most reducing experiments (Figure 6). Analyses of experimental glass VF257 yield an average FeO wt.% of 16.62, which exceeds the FeO* wt.% determined by EPMA (16.24 wt.% FeO*), yielding a non-physical average Fe^{3+}/Fe^{T} of −0.023. We include the data from VF257 as its range of uncertainty does extend into physical values of Fe^{3+}/Fe^{T}, but the negative result does not affect our interpretation of Fe redox of reduced magmas.

Table 1
Experimental Conditions and Summarized Results

Series	Experiment	Log f_{O2}	Loop	Temperature (°C)	Duration (h)	Fe^{3+}/Fe^{T} Mössbauer[b]	Fe^{3+}/Fe^{T} Wet chemistry[c]	XANES (eV)[a]
Time series	VF178	−4.68	Pt-Fe	1371	1	0.337 ± 0.003		7112.695 ± 0.043
	VF179	−4.74	Pt-Fe	1364	4	0.278 ± 0.004		
	VF188	−4.78	Pt-Fe	1360	12	0.234 ± 0.008		7112.562 ± 0.003
	VF187	−4.74	Pt-Fe	1364	24	0.254 ± 0.001		7112.562 ± 0.009
	VF196	−4.74	Pt-Fe	1364	1	0.255 ± 0.004	0.228 ± 0.045	7112.565 ± 0.018
	VF194	−4.78	Pt-Fe	1360	4	0.243 ± 0.005	0.254 ± 0.022	7112.538 ± 0.007
	VF203	−4.78	Pt-Fe	1360	12	0.261 ± 0.004	0.303 ± 0.004	7112.572 ± 0.013
	VF202	−4.77	Pt-Fe	1361	24	0.241 ± 0.003		7112.539 ± 0.016
f_{O2} series	VF257	−11.18	Re	1365	6	0.051 ± 0.012	−0.023 ± 0.041	
	VF252	−8.73	Pt-Fe	1365	24	0.111 ± 0.008	0.091 ± 0.027	7112.129 ± 0.007
	VF244	−8.20	Pt-Fe	1369	24	0.104 ± 0.006	0.089 ± 0.034	7112.111 ± 0.008
	VF230	−7.73	Pt-Fe	1365	6	0.094 ± 0.009		7112.149 ± 0.008
	VF247	−7.24	Pt-Fe	1375	24	0.130 ± 0.010	0.088 ± 0.039	7112.163 ± 0.005
	VF224	−6.72	Pt-Fe	1366	6	0.127 ± 0.011	0.063 ± 0.012	
	VF291	−6.21	Pt-Fe	1366	6	0.162 ± 0.009	0.183 ± 0.013	7112.397 ± 0.024
	VF255	−5.25	Pt-Fe	1365	24	0.180 ± 0.014	0.214 ± 0.030	7112.468 ± 0.057
	VF243	−4.48	Pt-Fe	1371	24	0.260 ± 0.005	0.202 ± 0.035	
	VF215	−4.21	Pt	1368	6	0.305 ± 0.002	0.363 ± 0.004	7112.639 ± 0.008
	VF213	−2.69	Pt	1370	6	0.486 ± 0.007	0.395 ± 0.013	7112.983 ± 0.013
	VF231	−0.68	Pt	1365	6	0.716 ± 0.013	0.728 ± 0.003	7113.317 ± 0.008
	VF232	−0.20	Pt	1365	6	0.768 ± 0.010	0.819 ± 0.009	7113.382 ± 0.015
Temperature series	VF271[d]	−0.68	Pt	1250	72			7113.425 ± 0.008
	VF267	−0.68	Pt	1300	24	0.736 ± 0.011	0.779 ± 0.026	
	VF268	−0.68	Pt	1400	6	0.695 ± 0.009	0.679 ± 0.052	7113.220 ± 0.016
	VF270	−0.68	Pt	1450	2	0.661 ± 0.007	0.661 ± 0.037	7113.264 ± 0.012
	VF274	−0.68	Pt	1500	1	0.643 ± 0.006	0.655 ± 0.006	7113.203 ± 0.005

[a]Pre-edge centroid energies calculated by fitting the Fe Ka pre-edge with a Lorentzian + Linear baseline and two Gaussian sub-peaks calculated in the Larix (Larch) software package (Newville, 2013). [b]Mössbauer spectra were collected at room-temperature and fitted with extended Voigt-based Fitting (xVBF). Values for glass Fe^{3+}/Fe^{T} were then corrected for recoil-free fraction by a correction factor of $C = 1.203$ (Roskosz et al., 2022). Uncertainties reflect the propagated uncertainties for calculated hyperfine parameters on absorption peak areas. [c]FeO concentrations (wt%) for a subset of glasses were determined via duplicate analyses using the Wilson (1960) colorimetric method at the University of Michigan (Analyst: R. Lange) and Fe_2O_3 concentrations were determined by difference from FeO* concentrations determined by WDS (Fe_2O_3 (wt%) = 1.1113(FeO* – FeO)). The relative proportion of FeO and Fe_2O_3 provide a basis for calculating Fe^{3+}/Fe^{T} and the uncertainties in the colorimetric technique and WDS analyses are propagated to determine uncertainties in Fe^{3+}/Fe^{T}. [d]Partially crystallized, not amenable to Mössbauer or wet chemical techniques.

3.3. XANES Spectra Fitting

Pre-edge energy centroid energies and their uncertainties for experiments characterized by XANES are listed in Table 1. A comparison of Fe^{3+}/Fe^{T} ratios (from both Mössbauer and wet chemistry) and pre-edge centroid energies exhibit non-linear increase from 7112.1 to 7113.5 eV for reduced to oxidized glasses. The Fe^{3+}/Fe^{T}-pre-edge centroid energy data for the Humphrey experiments form a trend similar to those for terrestrial basaltic glass standards (synthesized by Cottrell et al., 2009, Fe^{3+}/Fe^{T} values from Zhang et al., 2018) and the quadratic calibration curve calculated by Zhang et al. (2018; Figure 7).

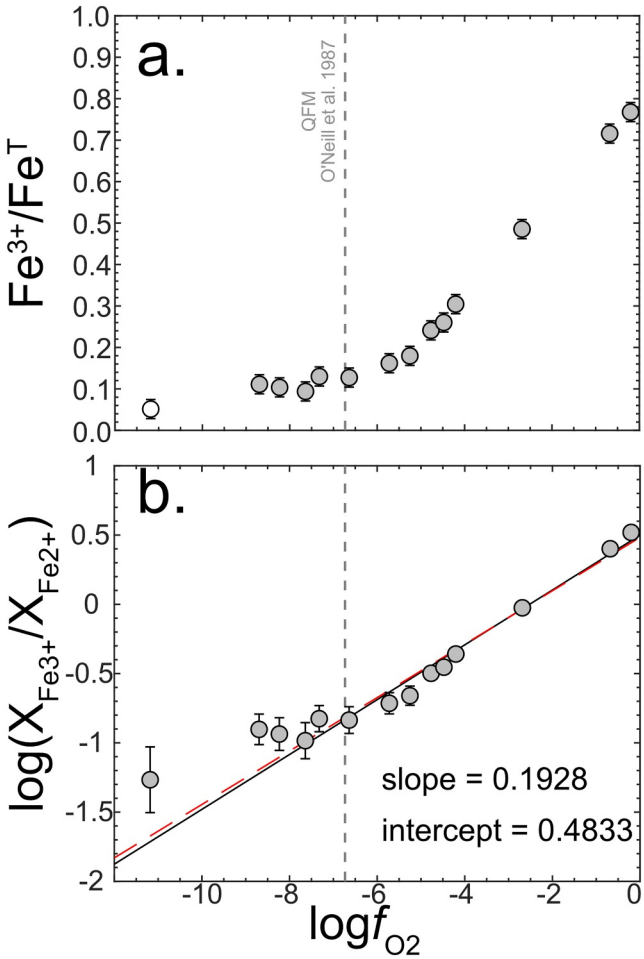

Figure 4. (a) Fe^{3+}/Fe^{T} ratio versus log f_{O2} and (b) log Fe^{3+}/Fe^{2+} versus log f_{O2} as determined by room-temperature Mössbauer spectroscopy for Humphrey glasses quenched from 1365°C to 100 kPa (circles). The transparent circle represents VF257 (Humphrey, log $f_{O2} = -11.18$), which appears to deviate from linearity when compared to other experiments. The weighted-least-squares best fit lines for all Humphrey f_{O2} series experiments ($n = 14$) and a regression with VF257 omitted ($n = 13$) are plotted as the black solid line and red-dashed lines, respectively, in panel (b). All error bars represent 2-σ. Symbols without error bars have uncertainties smaller than the symbol size. Vertical dashed is the QFM buffer (O'Neill, 1987).

4. Discussion

4.1. Comparison of Fe^{3+}/Fe^{T} From Mössbauer Spectroscopy and Wet Chemistry

Mössbauer spectroscopy and wet chemical are commonly utilized to quantify Fe^{3+}/Fe^{T} ratios in experimental glasses, but their relative merits and agreement are debated (Bézos et al., 2021; Cottrell & Kelley, 2011; Cottrell et al., 2009; Dingwell, 1991; Jayasuriya et al., 2004; Lange & Carmichael, 1989; Mysen et al., 1985; Ottonello et al., 2001; Righter et al., 2013; Wilke et al., 2005; Zhang et al., 2015). An advantage of Mössbauer spectroscopy is its superior precision relative to wet chemical colorimetry for Fe^{3+}/Fe^{T} determinations (Jayasuriya et al., 2004; Mysen et al., 1985; Wilke et al., 2005). However, Mössbauer can yield non-unique Fe^{3+}/Fe^{T} ratios depending on how features in the spectra are interpreted (Alberto et al., 1996; Berry et al., 2018; Cottrell et al., 2009; Matzen et al., 2022; Partzsch et al., 2004). Previous comparisons of Fe^{3+}/Fe^{T} ratios determined by Mössbauer and wet chemical methods (Cottrell et al., 2009; Cottrell & Kelley, 2011; Dingwell, 1991; Mysen et al., 1985; Wilke et al., 2005; Zhang et al., 2015) agree broadly (Figure 8.) but approaches to quantifying Mössbauer spectra for glasses have varied, especially with respect to applying Mössbauer correction factors accounting for recoil-free fractions of $^{57}Fe^{2+}$ and $^{57}Fe^{3+}$ (De Grave & Van Alboom, 1991; Lange & Carmichael, 1989; Morris et al., 1995, 2006; Righter et al., 2013; Roskosz et al., 2022; Zhang, 2022; Zhang et al., 2018). Here, we leverage our measurements of Fe^{3+}/Fe^{T} using both wet chemical colorimetry and conventional Mössbauer on the same subset of glasses to investigate the agreement between wet chemical colorimetry and our preferred Mössbauer fitting protocol.

Wet chemical and Mössbauer spectroscopic determination of Fe^{3+}/Fe^{T} scatter about the one-to-one line, with no apparent systematic offset between the two measurements. The goodness-of-fit between the two measurements is quantified using a modified χ^2 parameter accounting for both techniques' uncertainties with the form:

$$\chi^2 = \sum \frac{1}{\sigma_{MB}^2 + \sigma_{WC}^2}(MB - WC)^2, \quad (3)$$

where n represents the number of samples analyzed by both Mössbauer and wet chemistry ($n = 16$), MB and WC represent the Fe^{3+}/Fe^{T} ratios determined from Mössbauer spectroscopy and wet chemistry, respectively, and σ_i representing 2-σ uncertainty of MB and WC. This χ^2 parameter characterizes the goodness-of-fit of the data to a one-to-one line, treating the combined uncertainty of each datapoint as the resultant vector between the two error bars. As the uncertainties in both coordinates have the same units, this treatment of the resultant uncertainties is valid. Consequently, calculating the datapoint weight as being equal to the squared inverse of the uncertainty vector magnitude, is a fair assumption and does not require a more complicated model (e.g., York, 1968) for describing the weights.

An ideal distribution would converge to $\chi^2/n \equiv 1$. An initial calculation of $\chi^2/n = 5.03$ suggests either that the one-to-one model was inappropriate for the data, or that uncertainties are underestimated. We attribute this underfitting to the underestimation of Mössbauer uncertainties as they only account for errors between the lineshape used to fit the Mössbauer spectra, and not from uncertainty in the range of Fe^{3+}/Fe^{T} values obtained when authors use physically valid, yet different spectra fitting protocols (Berry et al., 2018; Cottrell et al., 2009; Matzen et al., 2022; Partzsch et al., 2004; Zhang et al., 2015, 2018). To account for the latter source of uncertainty, workers either assign their Mössbauer uncertainties to a uniform value, that is, large relative to the uncertainty of a single fitting model, typically ranging from 0.01 to 0.05 (Jayasuriya et al., 2004; Matzen et al., 2022; Morris

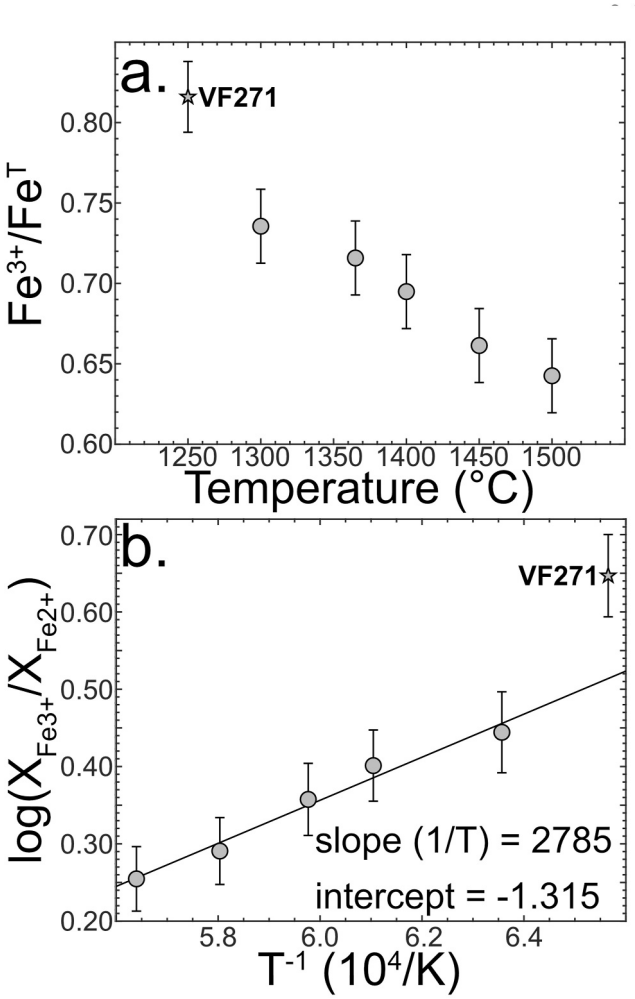

Figure 5. (a) Fe^{3+}/Fe^{T} ratios determined in the temperature series from room-temperature Mössbauer spectroscopy for Humphrey (gray circles) versus temperature (°C) and (b) versus inverse temperature (1/K). The Fe^{3+}/Fe^{T} ratio for glass from partially crystallized experiment VF271, (gray star) is approximated by XANES in Section 4.8.2 All experiments were conducted in air in air ($\log f_{O2} = -0.68$). Weighted linear regression of $\log\left(\frac{X_{Fe3+}}{X_{Fe2+}}\right)$ versus inverse temperature (not including VF271 owing to crystallization significantly modifying its glass composition) yields $\log\left(\frac{X_{Fe3+}}{X_{Fe2+}}\right) = \frac{2785 \pm 241.8\ K}{T} - 1.315 \pm 0.1437$; $R^2 = 0.976$.

et al., 2006; Mysen et al., 1985; Righter et al., 2013; Wilke et al., 2005), or rescale calculated Fe^{3+}/Fe^{T} uncertainties to optimize fit with an independent measure of Fe^{3+}/Fe^{T} (Cottrell et al., 2009). With the assumption that Mossbauer uncertainty is underestimated, we resize the Mössbauer uncertainty to $\sigma_{MB} = 0.023$, which reduces to $\chi^2/n = 1$, optimizing agreement between colorimetric wet chemistry and our Mössbauer fitting protocol. Following literature descriptions of resized Mössbauer uncertainties (Jayasuriya et al., 2004; Matzen et al., 2022; Morris et al., 2006; Mysen et al., 1985; Righter et al., 2013; Wilke et al., 2005), σ_{MB} is not described as being a multiple of standard deviations relative to a mean, so the value of 0.023 is not reported as 1 or 2 − σ.

In the following sections, we consider, only, Mössbauer determined Fe^{3+}/Fe^{T} to facilitate direct comparison between behavior of Humphrey melts to experiments of Righter et al. (2013) and Matzen et al. (2022), all corrected for recoil-free fraction from Roskosz et al. (2022).

4.2. Modeling Fe^{3+}/Fe^{2+} versus f_{O2} in Multicomponent Silicate Melts

To determine the Fe^{3+}/Fe^{2+} ratio in a basaltic melt, we consider the following reaction:

$$FeO_{melt} + \frac{1}{4}O_2 = FeO_{1.5melt}, \quad (4)$$

which relates the Fe^{3+}/Fe^{2+} ratio to f_{O2} by the equilibrium constant:

$$K = \frac{a_{FeO}}{a_{FeO_{1.5}} f_{O_2}^{\frac{1}{4}}}, \quad (5)$$

where a_i is the thermodynamic activities of the melt components, i. At a standard reference pressure of 100 kPa, this expands to

$$\log\left(\frac{a_{FeO_{1.5}}}{a_{FeO}}\right) = 0.25 \log f_{O_2} - \frac{-\Delta G_r^0}{RT\ln(10)}, \quad (6)$$

where ΔG_r^0 is the change in Gibbs free energy of reaction 1, R is the ideal gas constant, and T is temperature. Expanding (Equation 6) to isolate mole fractions of Fe^{2+} and Fe^{3+} instead of activities:

$$\log\left(\frac{X_{Fe3+}}{X_{Fe2+}}\right) = 0.25 \log f_{O_2} - \frac{-\Delta G_r^0}{RT\ln(10)} - \log\left(\frac{\gamma_{Fe3+}}{\gamma_{Fe2+}}\right), \quad (7)$$

where X_i and γ_i refer, respectively, to mole fractions and activity coefficients of the Fe^{2+} and Fe^{3+} melt components. This expression provides an analytical basis for the calculation of Fe^{3+}/Fe^{2+} ratios in silicate melts, provided that $-\Delta G_r^0$ and $\log\left(\frac{\gamma_{Fe3+}}{\gamma_{Fe2+}}\right)$ can be approximated confidently. However, approximating the $\log\left(\frac{\gamma_{Fe3+}}{\gamma_{Fe2+}}\right)$ term by expanding the γ_i terms with symmetric or asymmetric Margules-type formulations (i.e., Mukhyopadhyay et al., 1993) yields unwieldy equations with >36 terms in 8+ melt components, which would require regression across a population of multicomponent silicate glasses with known composition and Fe^{3+}/Fe^{T} (Borisov et al., 2015; Jayasuriya et al., 2004; Sack et al., 1981). The number of viable experiments on natural (Fudali, 1965; Kilinc et al., 1983; Kress & Carmichael, 1988, 1991; Sack et al., 1981) and synthetic compositions (Borisov et al., 2013, 2015, 2017, 2018; Jayasuriya et al., 2004; Kennedy, 1948; Thornber et al., 1980) is small (*ca* 500 glasses) relative to the number of terms requiring fit coefficients. For this reason, models relating Fe^{3+}/Fe^{T} to f_{O2}, temperature, and composition are normally constructed with simpler empirical functions.

Table 2
Results From Colorimetric Analyses

Standard	FeO						Average	Reference
W-2a[a]	8.02[1]	8.30[2]	8.39[3]	8.39[4]	8.36[5]	8.30[6]	8.29 ± 0.14	8.34
SY-4[b]	2.89[1]	2.66[2]	2.88[3]	2.83[4]	2.95[5]	2.77[6]	2.83 ± 0.10	2.86

	FeO[c]					
Experiment	1.	2.	3.	FeO average	FeO*[d]	Fe^{3+}/Fe^{T}
VF196	13.29[1]	11.57[4]		12.43 ± 0.70	16.09 ± 0.23	0.228 ± 0.045
VF194	12.80[1]	11.89[4]	12.04[5]	12.24 ± 0.34	16.41 ± 0.13	0.254 ± 0.022
VF203	11.44[3]	11.58[5]		11.51 ± 0.06	16.50 ± 0.03	0.303 ± 0.004
VF257	17.44[2]	15.80[4]		16.62 ± 0.67	16.24 ± 0.03	−0.023 ± 0.041
VF252	14.55[1]	13.57[4]		14.06 ± 0.40	15.47 ± 0.14	0.091 ± 0.027
VF244	15.71[1]	14.36[4]		15.04 ± 0.55	16.51 ± 0.11	0.089 ± 0.034
VF247	14.77[1]	13.34[4]		14.06 ± 0.58	15.41 ± 0.18	0.088 ± 0.039
VF224	14.57[1]	14.20[5]		14.39 ± 0.15	15.35 ± 0.10	0.063 ± 0.012
VF291	11.00[3]	10.90[5]	10.66[6]	10.85 ± 0.12	13.28 ± 0.14	0.183 ± 0.013
VF255	12.60[1]	11.52[4]		12.06 ± 0.44	15.34 ± 0.17	0.214 ± 0.030
VF243	13.26[1]	11.94[4]		12.60 ± 0.54	15.80 ± 0.16	0.202 ± 0.035
VF215	10.52[1]	10.45[4]		10.49 ± 0.03	16.46 ± 0.10	0.363 ± 0.004
VF213	9.38[1]	9.88[2]		9.63 ± 0.20	15.92 ± 0.08	0.395 ± 0.013
VF231	4.38[1]	4.30[2]		4.34 ± 0.03	15.94 ± 0.13	0.728 ± 0.003
VF232	3.09[1]	2.74[4]		2.92 ± 0.14	16.14 ± 0.13	0.819 ± 0.009
VF267	2.86[2]	3.80[5]		3.33 ± 0.38	15.04 ± 0.03	0.779 ± 0.026
VF268	3.84[2]	5.75[4]		4.80 ± 0.78	14.94 ± 0.15	0.679 ± 0.052
VF270	4.37[2]	5.71[4]		5.04 ± 0.55	14.87 ± 0.09	0.661 ± 0.037
VF274	5.23[3]	5.28[3]	5.04[3]	5.18 ± 0.09	15.04 ± 0.07	0.655 ± 0.006

Note. All uncertainties reported as $1-\sigma$. [a]Flanagan and Kirschenbaum (1984). [b]Bowman (1995). [c]Averages of FeO values from individual colorimetric analyses. [d]FeO* (all Fe as Fe^{2+}) from EPMA analysis. [1–6] Individual analytical sessions.

A commonly used expression relating Fe^{3+}/Fe^{2+} to f_{O2}, temperature, and composition developed by Sack et al. (1981) has the form:

$$\log\left(\frac{X_{Fe3+}}{X_{Fe2+}}\right) = k\log f_{O_2} + \frac{h}{T} + c + \sum d_i X_i, \quad (8)$$

where k, h, c, and d_i are coefficients derived from regression of experiments and the summation is over melt oxide mole fractions, X_i, ($i = SiO_2$, TiO_2, MgO, etc). In Equation 4, k is treated as a variable rather than the fixed coefficient of 0.25 in Equation 3. The latter would apply if interactions between Fe^{2+} and Fe^{3+} in the melt were thermodynamically ideal, but studies of multicomponent silicate liquids have repeatedly found that the empirical correlation between $\log\left(\frac{X_{Fe3+}}{X_{Fe2+}}\right)$ and $\log f_{O2}$ has a slope smaller than 0.25, with consequent values of k from 0.18 to 0.22 (Fudali, 1965; Jayasuriya et al., 2004; Kress & Carmichael, 1988, 1991; Sack et al., 1981). The value of k smaller than 0.25 attests to non-ideal Fe^{2+}-Fe^{3+} interactions in the melt, and the deviation from 0.25 is expected to increase with increasing Fe in a melt (Jayasuriya et al., 2004). An alternative approach is to parameterize expressions that fix the k coefficient to 0.25 and account for Fe species' non-ideality by fitting more complex expressions estimating the $\log\left(\frac{\gamma_{Fe3+}}{\gamma_{Fe2+}}\right)$ term (Jayasuriya et al., 2004). However, Jayasuriya et al. (2004) demonstrated that such expressions may be less accurate than empirical fits similar to Equation 4, even when both expressions

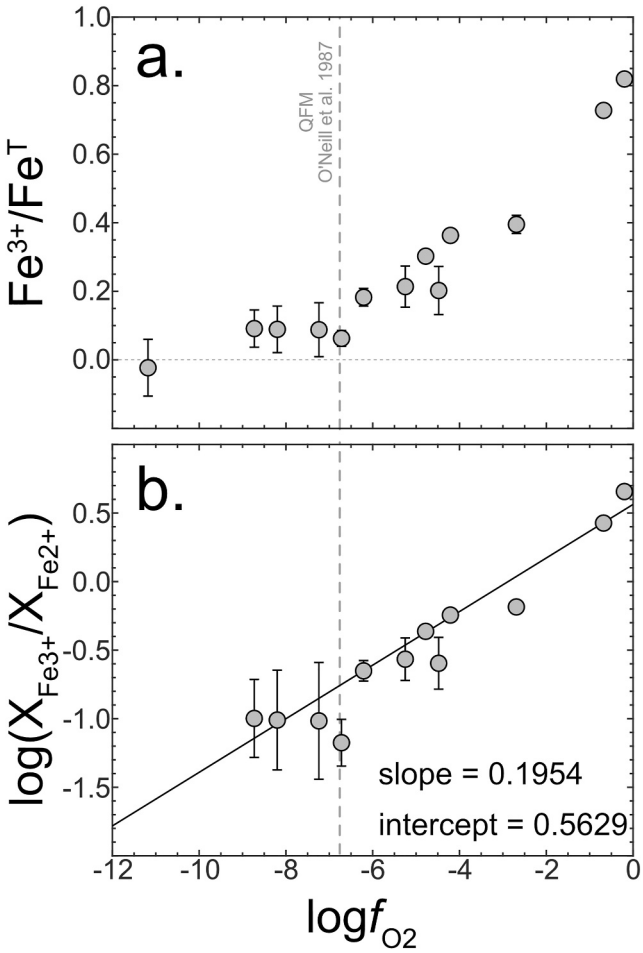

Figure 6. (a) Fe^{3+}/Fe^{T} versus $\log f_{O2}$ and (b) versus $\log f_{O2}$ as determined by wet-chemical methods for Humphrey glasses quenched from 1365°C to 100 kPa (gray circles). The weighted-least-squares best fit line: $0.1954 \pm 0.0084 \times \log f_{O_2} + 0.5629 \pm 0.0294$; $R^2 = 0.912$ Is plotted as a black line along with the data in (b). Error bars represent the 2-σ deviation established from replicated analyses. Symbols without error bars have uncertainties smaller than the symbol size. The vertical dashed line is the QFM buffer (O'Neill, 1987).

are derived from the same set of experiments. Consequently, we employ regressions based on the Sack et al. (1981) form as expressed by Equation 8.

The empirical models that employ this general form (e.g., Borisov et al., 2018; Jayasuriya et al., 2004; Kress & Carmichael, 1991) have proved accurate for melt compositions similar to those from which they are calibrated. Among these, Borisov et al. (2018)'s model is likely the most robust, owing to its large ($n = 434$) and diverse calibration database. However, this subset of experimental data is compositionally distinct from martian igneous lithologies (Figure 1; Borisov et al., 2018; Filiberto, 2017; Righter et al., 2013), which are more Fe-rich and Al-poor compared to compositions in these earlier models.

If elevated Fe in martian magmas relative to terrestrial magmas contributes to greater non-ideality of Fe^{3+} – Fe^{2+} interactions, then coefficient, k, in Equation 8 could be smaller for martian magmas compared to those from calibrations from less Fe-enriched compositions. The correlation between $\log\left(\frac{X_{Fe3+}}{X_{Fe2+}}\right)$ versus $\log f_{O2}$ for Fe-rich Humphrey yields a slope of 0.1968 ± 0.0104 ($1-\sigma$), which is at the low end but similar to those found in previous models (0.18–0.22). In the following sections, we investigate the determination of Fe^{3+}/Fe^{T} in superliquidus 100-kPa gas-mixing furnace experiments on martian basalt compositions across the literature to better understand the k value applicable to martian magmas.

4.3. A New Model for Fe^{3+}/Fe^{T} Versus f_{O2} for Martian Magmas

Using Fe^{3+}/Fe^{T} ratio determinations from our f_{O2} and temperature experimental series and also from experiments of Righter et al. (2013) on a Zagami analog (sherg1) and Matzen et al. (2022) on an alkali-free Gusev Crater basalt, Homeplate, we construct a predictive model by conducting multiple linear regression analysis where observations of $\log\left(\frac{X_{Fe3+}}{X_{Fe2+}}\right)$, weighted by the squared inverse of their uncertainties, are regressed against a combination of $\log f_{O2}$, $1/T$, and different compositional components. Compositional components included in our model were determined using weighted stepwise regression with 95% and 90% confidence intervals for entry and removal, respectively, via MATLAB's "stepwiselm" function (The MathWorks Inc, 2020). The stepwise regression produces a linear model where $\log\left(\frac{X_{Fe3+}}{X_{Fe2+}}\right)$ is predicted by,

$$\log\left(\frac{X_{Fe3+}}{X_{Fe2+}}\right) = 0.1988 \log f_{O_2} + \frac{3775}{T} - 1.753 - 99.62X_{K_2O}, \quad (9)$$

with X_{K2O} being the only statistically significant compositional term. Compared to Equation 9, previous models include more compositional terms, reflecting the smaller compositional variability in the martian-specific data compared to that used to calibrate other studies (e.g., Equation 9, 41 experiments; Borisov et al., 2018, 434 experiments). The significance of K_2O is consistent with previous regressions (e.g., Borisov et al., 2018; Jayasuriya et al., 2004; Kress & Carmichael, 1991; Righter et al., 2013), however, it is relatively more pronounced, suggesting that the cumulative contribution from all oxide components is represented by differences in K_2O. It is anticipated that consideration of a more compositionally diverse and larger data set would yield a model with greater constraints on the influence of composition and that the large apparent dependence on K_2O concentration would be diminished.

As quantified by the unreduced χ^2 goodness-of-fit parameter calculated based on predicted versus observed Fe^{3+}/Fe^{T}, the model presented in Equation 9 fits the martian-relevant experimental data better than more complex

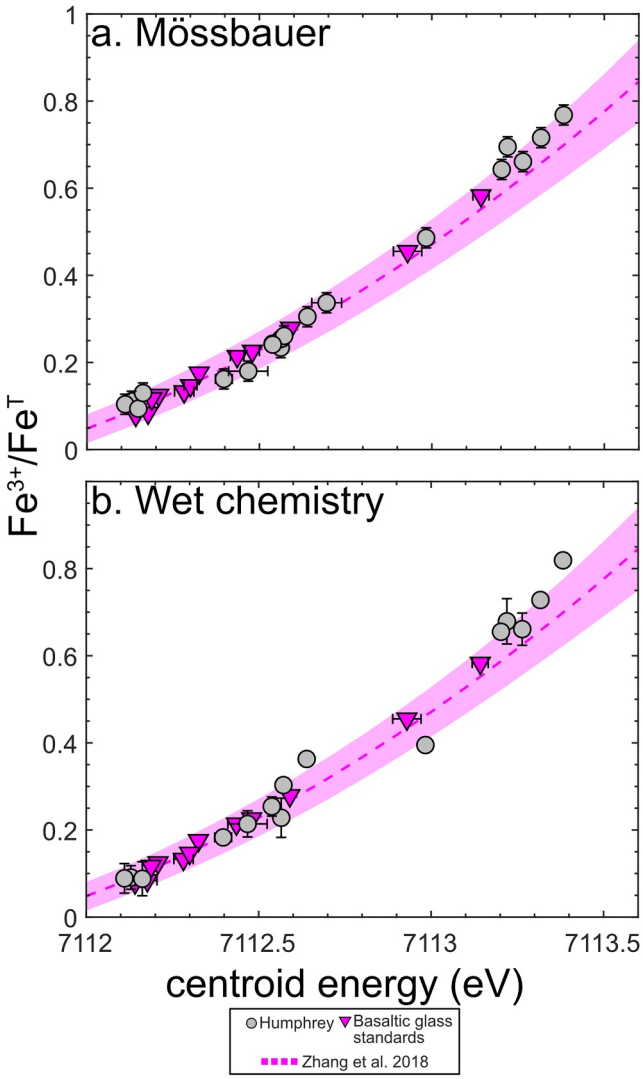

Figure 7. Pre-edge centroid energies from XANES spectra versus Fe^{3+}/Fe^{T} determined by (a) Mössbauer spectroscopy and (b) wet chemistry. The pre-edge centroid energies of basaltic glass standards (magenta upside-down triangles; synthesized by Cottrell et al., 2009, analyzed in the present study) are plotted against their Fe^{3+}/Fe^{T} as characterized by Zhang et al., 2018. The quadratic fit and associated 95% confidence intervals for terrestrial basalt regressed by Zhang et al., 2018 are denoted by the magenta dashed line and field.

models from Kress and Carmichael (1991), Jayasuriya et al. (2004), Borisov et al. (2018), as well as the martian-specific parameterization from Righter et al. (2013) suggesting that the dependence of $\log\left(\frac{X_{Fe3+}}{X_{Fe2+}}\right)$ on $\log f_{O2}$ and temperature for all previously investigated magmas is different than observed for martian magmas (Figure 10).

4.4. Alternate Models

Another modeling approach is to regress new coefficients to a relationship with the form of Equation 8 using the oxide parameters previously identified by similar examples (Borisov et al., 2018; Hirschmann, 2022; Jayasuriya et al., 2004; Kilinc et al., 1983; Kress & Carmichael, 1991; Sack et al., 1981). While this inevitably introduces terms that are not statistically significant at a 95% confidence interval, it allows construction of a more complicated model taking into account compositional terms that have been found to be significant when fitting a broader diversity of melt compositions (Table 3 and Figure S1 in Supporting Information S1).

We also parameterized 2043 additional linear models that incorporate the remaining possible combinations of the 11 compositional components used by these established models and compared the resulting reduced chi-square goodness of fit, calculated based on predicted versus observed Fe^{3+}/Fe^{T} in the resulting models. The model that performs best is:

$$\log\left(\frac{X_{Fe3+}}{X_{Fe2+}}\right) = 0.2133\log f_{O_2} + \frac{4370}{T} - 9.118 + 11.96X_{SiO_2} + 110.4X_{Al_2O_3} - 6.875X_{Na_2O} - 184.6X_{SiO_2}X_{Al_2O_3} \quad (10)$$

with a reduced χ^2 goodness-of-fit ~1.22 (Figure 9 and Table 3). This expression includes terms describing the role of multiple major oxide components and has a smaller reduced χ^2 goodness-of-fit than Equation 9, but many terms were not found to be statistically significant, suggesting that this model may be overfit to the calibration data set and may not extrapolate to other martian magma compositions accurately. Interestingly, though K_2O was found to be significant in Equation 9, it is not selected as a statistically significant compositional coefficient in Equation 10. This further demonstrates that further compositional variance needs to be explored to confidently define the interactions between Fe and various compositional components.

4.5. Comparing Models Characterizing Fe^{3+}/Fe^{T} in Magmas

Comparison of experimental results on Humphrey and other martian compositions to our new models and those parameterized to describe Fe^{3+}/Fe^{T} versus f_{O2}, temperature, and composition allow evaluation of their relative success in predicting Fe^{3+}/Fe^{T} ratios for martian basalts. As shown in Figure 9, the newly calibrated models (Equations 9 and 10) reproduce the experiments better than previous expressions (Borisov et al., 2018; Jayasuriya et al., 2004; Kress & Carmichael, 1991; Righter et al., 2013). This is unsurprising, given that the former were calibrated on the comparison data set. Among the previous models, both the Kress and Carmichael (1991) and Borisov et al. (2018) expressions reproduce the data well for Humphrey, but not as favorably for the Shergottite or Homeplate data. Righter et al. (2013)'s martian-specific parameterization accurately predicts the Fe^{3+}/Fe^{T} of their experiments but does not accurately describe Humphrey and Homeplate data, highlighting the importance of investigating a wide range of compositional diversity to optimize model accuracy.

Considering all 2048 models parameterized on our data set of martian magma experiments, the correlation between $\log\left(\frac{X_{Fe3+}}{X_{Fe2+}}\right)$ on $\log f_{O2}$, quantified by k ranges from ~0.19 to 0.22. These k values are consistent with those

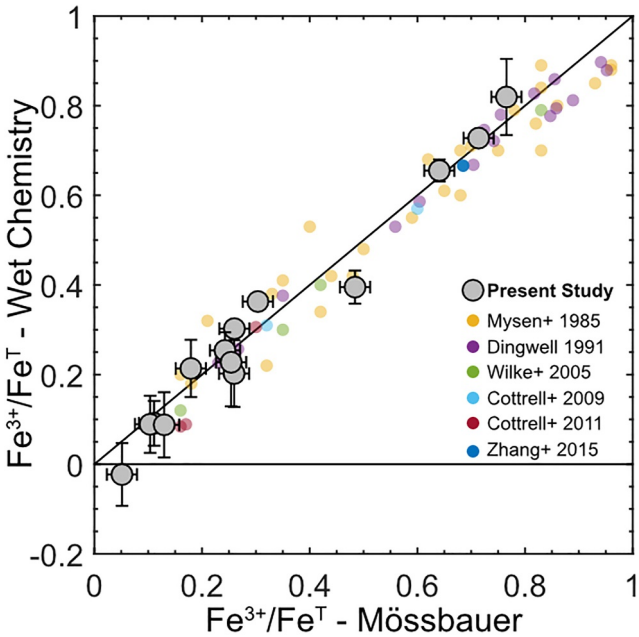

Figure 8. A comparison of wet chemical and Mössbauer spectroscopic determinations of Fe^{3+}/Fe^{T} ratios for Humphrey ($n = 19$) and experimentally synthesized silicate glasses (Mysen et al., 1985, $n = 28$; Dingwell, 1991, $n = 16$; Wilke et al., 2005, $n = 4$; Cottrell et al., 2009, $n = 3$; Cottrell & Kelley, 2011, $n = 4$, and Zhang et al., 2015, $n = 1$). Wet chemistry Fe^{3+}/Fe^{T} error bars are displayed as 2-σ and Mössbauer error bars are all set to 0.023 for Humphrey data. Solid line 1:1 line is shown.

parameterized in previous models (i.e., Borisov et al., 2018; Jayasuriya et al., 2004; Kress & Carmichael, 1991; Righter et al., 2013) and significantly lower than the theoretical value of 0.25 derived from the stoichiometry of Reaction 1 (Figure 10). The consistency between the k values regressed from the martian glasses and those from previous models provides no evidence that this non-ideality is enhanced for FeO*-rich (15–20 wt.%) martian magmas. The temperature dependence of Equations 9 and 10 is greater than modeled by Kress and Carmichael (1991), Jayasuriya et al. (2004), and Borisov et al. (2018), suggesting an increased sensitivity in $\log\left(\frac{X_{Fe3+}}{X_{Fe2+}}\right)$ as a function of temperature. Righter et al. (2013) also noted a deviation in the temperature dependence from existing models, albeit at a more extreme magnitude, suggesting that the smaller h coefficient implies that temperature variations may have a greater role in explaining f_{O2} variations between martian igneous lithologies formed from different parental melts.

4.6. Effect of Sulfur

The gas mixing experiments constraining Fe^{3+}/Fe^{T} for martian basalts presented here and in previous studies (Matzen et al., 2022; Righter et al., 2013) did not incorporate sulfur, which may be comparatively abundant in martian magmas (Ding et al., 2014) and which may affect ferric-ferrous equilibria (e.g., Saper et al., 2024). Under reducing to moderately reducing conditions relevant to martian basalts, sulfur should be present as S^{2-}, which is strongly associated with magmatic Fe^{2+}. Therefore, at a given f_{O2}, sulfur-enrichment will lower magmatic Fe^{3+}/Fe^{T}, as seen experimentally by comparison between sulfur-bearing melt inclusions and correlative sulfur free experimental melts (Saper et al., 2024).

If appreciable Fe^{2+} is associated with an FeS species, the homogeneous equilibrium between FeO and Fe_2O_3 species, as documented by the present experiments and described by Equations 9 and 10, would not accurately describe the Fe^{3+}/Fe^{T} ratio in the silicate melt. Assuming that the homogeneous equilibrium between Fe-oxide species is unaffected by the solution of modest amounts of FeS, then the Fe^{3+}/Fe^{T} would instead be given by

$$Fe^{3+}/Fe^{T} = FeO_{1.5}/(FeO_{1.5} + FeO + FeS). \quad (11)$$

As shown in Data set S3, this will produce a small decrease in Fe^{3+}/Fe^{T}, under oxidizing conditions, but has negligible effect under reducing conditions applicable to martian basalt petrogenesis.

4.7. Implications for Martian Magmatism

The models developed in Equations 9 and 10 allow the calculation of Fe valences in martian magmas at the f_{O2}s recorded by oxybarometry of martian igneous rocks at 100 kPa (i.e., near-surface pressures on Mars). This in turn facilitates the evaluation of the extent of Fe-redox mass transfer required to account for observed f_{O2} variations recorded in martian igneous rocks. We begin by considering the depleted, intermediate, and enriched shergottites (Symes et al., 2008), which comprise the class of meteorites for which f_{O2} variations between and within individual lithologies are most pronounced (Castle & Herd, 2017; Herd, 2019).

4.7.1. Superliquidus f_{O2} Evolution

To evaluate the effect of f_{O2} on magmatic Fe^{3+}/Fe^{T} ratios, we consider three different shergottite compositions: the parental magma composition of a depleted shergottite, Tissint, calculated by Castle and Herd (2017), the composition of a melt vein present in intermediate shergottite NWA 1068, which closely matches the composition of the bulk rock (Gross et al., 2013), and the bulk rock composition of enriched shergottite NWA 6234 (Barrat et al., 2002). For each, we take the f_{O2} representative of their early crystallization, as measured via the olivine-orthopyroxene-spinel oxybarometer (Sack & Ghiorso, 1989, 1994a, 1994b, 1994c), and quantify their Fe^{3+}/Fe^{T} ratios at 100 kPa and liquidus temperatures, as estimated at 100 kPa and f_{O2} = IW (~QFM-3.4;

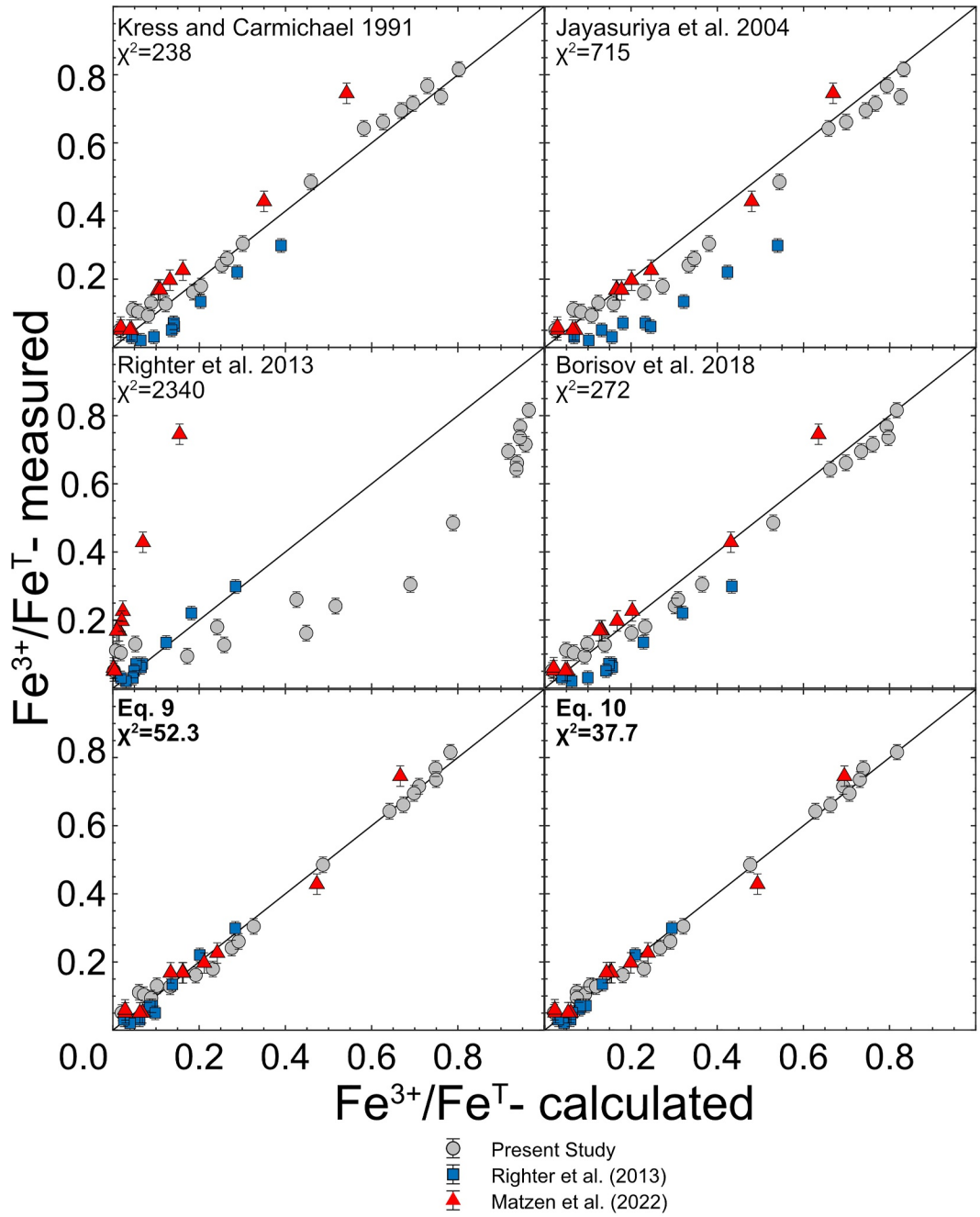

Figure 9. Comparison of measured Fe^{3+}/Fe^{T} for sherg1 (blue squares; Righter et al., 2013), Homeplate (red triangles, Matzen et al., 2022), and Humphrey (gray circles, present study) experiments to predicted values from parameterizations from Kress and Carmichael (1991), Jayasuriya et al. (2004), Borisov et al. (2018), Righter et al. (2013), and the models presented in Equations 9 and 10 of this study. Solid 1:1 line is shown.

O'Neill & Pownceby, 1993) in Rhyolite-MELTS (Gualda et al., 2012, 2015). We do the same for the f_{O2}s recorded in the later stages of crystallization, as quantified by groundmass assemblages of olivine-orthopyroxene-spinel or titanomagnetite-ilmenite (Ghiorso & Evans, 2008). The resulting variations are, respectively (Table 4) for Tissint, NWA 6234, and NWA 1060/1100, oxidized from QFM-3.5–QFM-1.4 (Castle & Herd, 2017), oxidized from QFM-2.8–QFM+1.2 (Gross et al., 2013), and oxidized from QFM-2.6–QFM+0.4 (Herd, 2006). As an initial assumption that Fe^{2+}–Fe^{3+} oxidation experienced by the magma was isothermal, isobaric, and otherwise isochemical, increases in Fe^{3+}/Fe^{T} ratios corresponding to these f_{O2}s

Table 3
Fit Parameters for Models Parameterized in This Study Along With Parameters for New Models Utilizing Compositional Components From Existing Models

Variable	KC91[a]	J04[b]	R13[c]	B18[d]	Equation 9	Equation 10
k (log f_{O2})	0.2114 (0.0069)	0.2112 (0.0079)	0.2114 (0.0072)	0.2118 (0.010)	0.1988 (0.0054)	0.2133 (0.0072)
h (1/T)	3809 (620.6)	3751 (848.1)	3803 (651.3)	3119 (1028)	3775 (635.1)	4370 (784.2)
c	−2.235 (0.8146)	−2.148 (1.187)*	−2.222 (0.9030)	−1.885 (6.433)**	−1.753 (0.3739)	−9.118 (3.030)
d_{SiO2}				0.9613 (11.83)**		11.96 (5.239)
d_{TiO2}				−42.53 (39.19)**		
d_{Al2O3}	3.463 (5.497)**	3.769 (6.585)**	3.442 (5.617)**			110.4 (47.44)
d_{MgO}		−0.2680 (2.689)**		−1.967 (34.24)**		
d_{CaO}	5.325 (2.844)*	5.021 (4.115)**	5.286 (3.098)*	8.273 (6.951)**		
d_{Na2O}	−3.803 (1.889)	−3.728 (3.291)**	−3.880 (2.872)**	−5.111 (4.041)**		−6.875 (2.286)
d_{K2O}	−72.77 (132.4)**	−75.54 (143.5)**	−71.92 (136.6)**	−225.2 (198.1)**	−99.62 (31.06)	
d_{P2O5}		1.866 (30.42)**	1.003 (28.71)**	−5.996 (36.82)**		
d_{SiAl}				−0.4263 (15.95)**		−184.6 (83.28)*
d_{SiMg}				1.198 (64.50)**		
d_{FeO*}	−0.8074 (1.889)**	−0.8186 (2.155)**	−0.8382 (2.112)**			
Reduced X^2	1.524	1.666	1.592	1.480	1.461	1.179

Note. Estimates of fit value ±1 standard error. [a–d] Parameterizations which adopt compositional terms from Kress and Carmichael (1991), Equation 7, Jayasuriya et al. (2004), Equation 12, Borisov et al. (2018), Equation 4, and Righter et al. (2013), Equation 2 as the d_i terms for the (Sack et al., 1981) form (Equation 8, this study) and regressing the martian basalt experiment results to calculate new coefficients. * Term is significant at a confidence interval between 90% and 95%. ** Term is not significant at 90% confidence interval.

evolutionary paths were calculated. This calculation allows for comparison of Fe^{3+}/Fe^{T} values across different f_{O2} for the same magma composition depending on the model used to approximate Fe^{3+}/Fe^{T} versus f_{O2}, temperature, and composition.

Increases in f_{O2} for Tissint, NWA 6234, and NWA 1068/1100 correspond to $\Delta Fe^{3+}/Fe^{T}$ (i.e., final Fe^{3+}/Fe^{T} – initial Fe^{3+}/Fe^{T}) = 0.048, 0.177, 0.044 according to Equation 9 and 0.007, 0.021, 0.029 according to Equation 10, respectively. The systematically larger $\Delta Fe^{3+}/Fe^{T}$ calculated for f_{O2} evolution, as calculated for Equation 9 versus Equation 10 is reflective of the greater initial Fe^{3+}/Fe^{T} ratios predicted by Equation 9 and implies that the magmas would require greater mass transfer processes to reach the final f_{O2} than required by Equation 10. These results provide quantitative insight into how changes in log f_{O2} observed for martian magmas require much less mass transfer than comparatively oxidized terrestrial basalt. Notably, the $\Delta Fe^{3+}/Fe^{T}$ of 0.044–0.177 that corresponds to 2.1–4 Δlog f_{O2} increases in the shergottite magmas (calculated via Equation 9) would oxidize an average MORB composition (White & Klein, 2014) at QFM (O'Neill, 1987), 1350°C, and 100-kPa by 0.72–2.25 Δlog f_{O2} according to Borisov et al. (2018)'s model. We compare the Fe^{3+}/Fe^{T} evolutionary paths predicted by Equations 9 and 10 to the models of Kress and Carmichael (1991), Jayasuriya et al. (2004), Righter et al. (2013), and Borisov et al. (2018) across the same range of f_{O2} to investigate the difference in model behaviors (Figure 11). The Fe^{3+}/Fe^{T} curve for Equation 9 plots closely to Jayasuriya et al. (2004) and Borisov et al. (2018) for Tissint and NWA 6234, while Equation 10 plots close to Righter et al. (2013). The curves from Equations 9 and 10 plots close to the Righter et al. (2013) model for NWA 1068. The relatively shallow curves predicted by Equation 10 and Righter et al. (2013) models provide a simple explanation for the f_{O2} variations observed: that large differences in f_{O2} for martian magmas may require only

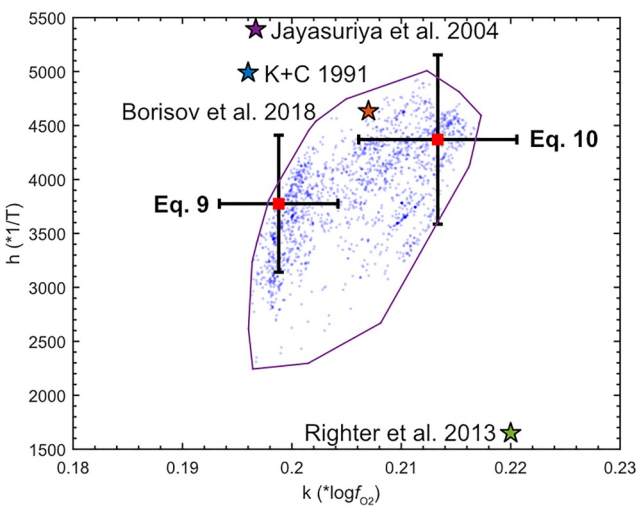

Figure 10. Comparison of k and h coefficients in Equations 9 and 10 parameterized for martian magma compared to Kress and Carmichael (1991), Jayasuriya et al. (2004), Borisov et al. (2018), and Righter et al. (2013). k and h fit coefficients for the 2046 remaining combinations of compositional components (see Section 4.5) are represented by blue dots in purple polygon.

Table 4
Shergottite Compositions, Liquidus Temperatures, Initial and Final f_{O2} Values Used for Calculation of Fe^{3+}/Fe^{T}

Shergottite compositions	Depleted Tissint[a]	Intermediate NWA 6234[b]	Enriched NWA 1068/1100[c]
SiO_2	47.2	44.54	45.78
TiO_2	0.67	1.13	0.77
Al_2O_3	5.2	4.86	5.75
Cr_2O_3	0.44	1.04	0.63
FeO*	21.6	23.77	20.48
MnO	0.56	0.58	0.46
MgO	16	17.01	16.50
CaO	7	6.15	7.91
Na_2O	0.77	0.9	1.14
K_2O	0.02	0.07	0.16
P_2O_5	0.51	0.82	0.42
total	99.97	100.87	100
Isothermal[d]			
Temperature (°C)	1400[a]	1468[e]	1401[e]
f_{O2} evolution (QFM-relative)	−3.5 → −1.4[a]	−2.8 → +1.2[b]	−2.6 → +0.4[f]
Fe^{3+}/Fe^{T} evolution (Equation 9)	0.032 → 0.080	0.043 → 0.220	0.016 → 0.060
Fe^{3+}/Fe^{T} evolution (Equation 10)	0.004 → 0.011	0.003 → 0.024	0.009 → 0.038
Isochemical cooling[g]			
Temperature evolution (°C)	1400 → 1100	1468 → 1100	1401 → 1100
f_{O2} evolution (Equation 9)	−3.5 → −2.7	−2.8 → −1.9	−2.6 → −1.8
f_{O2} evolution (Equation 10)	−3.5 → −2.9	−2.8 → −2.1	−2.6 → −2.0

[a]Parental magma composition, liquidus temperature, and f_{O2} estimates from Castle and Herd (2017). [b]Melt vein composition and f_{O2} estimates for NWA 6234 from Gross et al. (2013). [c]Bulk rock composition for NWA 1068/1100 from Barrat et al. (2002). [d]Scenario estimating $\Delta Fe^{3+}/Fe^{T}$ to account for f_{O2} evolution in shergottite melts (Section 4.7; Figure 11). [e]Liquidus temperature calculated at 100 kPa and f_{O2} = IW in Rhyolite-MELTS (Gualda et al., 2012, 2015). [f]f_{O2} estimates for NWA 1068/1100 from Herd (2006). [g]Scenario estimating Δf_{O2} during isochemical cooling of shergottite melts (Section 4.7; Figure 12).

small $\Delta Fe^{3+}/Fe^{T}$ across all f_{O2}. However, as Equation 10 is overfit to the calibration data set and Fe^{3+}/Fe^{T} ratios calculated by the Righter et al. (2013) model do not accurately predict Fe^{3+}/Fe^{T} ratios of the experimentally synthesized martian magmas from the current study or those of Matzen et al. (2022) (Figure 8), the Fe^{3+}/Fe^{T} evolution curves for Equation 9 are likely better for evaluating Fe^{3+}/Fe^{T} for Tissint, NWA 6234, and NWA 1068/1100.

4.7.2. Cooling-Related Oxidation of Martian Basaltic Magmas

The above calculation indicates how much oxidation of FeO to Fe_2O_3 would be required to account for the f_{O2} evolution observed in martian igneous rocks. Another approach is to estimate the effects of magmatic differentiation on oxygen fugacity. These effects include Fe^{3+}/Fe^{T} fractionation associated with crystallization, degassing, assimilation, decompression, and changes in f_{O2} owing to isochemical (constant magma composition and Fe^{3+}/Fe^{T} ratio) cooling. Investigating the collective effects of all of these is beyond the scope of the present study, but the model presented here allows us to calculate the isolated effect of temperature change on f_{O2} by modeling unbuffered, isochemical cooling of shergottitic magmas (Figure 12). Assuming that the shergottites retain the initial Fe^{3+}/Fe^{T} estimated by models prior to cooling, cooling of Tissint, NWA 6234, and NWA 1068/1100 from their liquidus temperatures to 1100°C results in f_{O2} shifts relative to QFM of 0.8, 0.9, and 0.8 log units according to Equation 9 and 0.6, 0.7, and 0.6 log units according to Equation 10 (Table 4). Thus, a significant

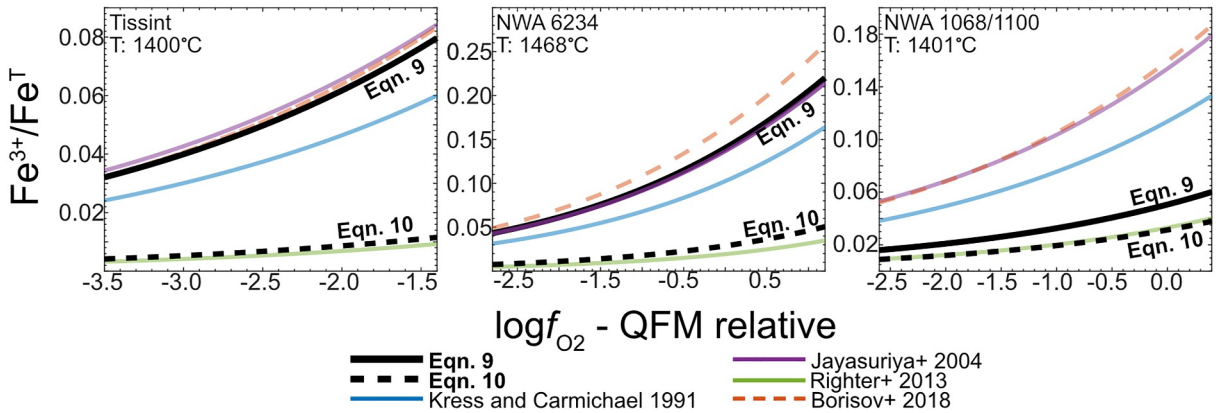

Figure 11. Comparison of predicted change in Fe^{3+}/Fe^{T} required to explain the change in f_{O2} as recorded in olivine shergottites Tissint (Castle & Herd, 2017), NWA 6234 (Gross et al., 2013), and NWA 1068/1100 (Herd, 2006) from different models: Equation 9—derived via stepwise regression; Equation 10—derived by combining compositional components that reduce χ^2 between observed and measured Fe^{3+}/Fe^{T}; Kress and Carmichael (1991); Jayasuriya et al. (2004); Righter et al. (2013); Borisov et al. (2018). As discussed in the text, Equation 9 is the model best suited to describe Fe^{3+}/Fe^{T} versus f_{O2} variations in the shergottite magmas.

fraction of the f_{O2} increase evident along the cooling path of martian meteorites (respectively, 2.1, 4.0 and 3.0 log units relative to QFM) can be attributed to cooling alone.

The f_{O2} change during isochemical cooling calculated with Equations 9 and 10 is different from and more pronounced than that predicted by the models of Kress and Carmichael (1991), Jayasuriya et al. (2004), or Borisov et al. (2018)'s. The former two predict about ~0.5 log units decreased f_{O2} relative to QFM during the cooling interval and the latter one predicts ~0.3 log units increased f_{O2}. Differences in the predicted f_{O2}-temperature paths are due to the smaller h coefficient in Equation 8 regressed for the martian magmas (Equations 9 and 10) relative to models derived from non-martian compositions (Figure 10). Although we do not consider the effects of crystallization during magmatic evolution on the f_{O2}, crystallization of olivine, and probably other mafic silicates, would enrich melt Fe^{3+}/Fe^{T} and increase f_{O2} (Aithala & Hirschmann, 2024; Castle & Herd, 2017; Peslier et al., 2010), further lessening the extent to which mass transfer processes are needed to increase melt Fe^{3+}/Fe^{T}. This expectation reinforces the conclusions from the isochemical exercises above, that increases in martian magma f_{O2} are achievable with relatively small amounts of mass transfer compared to terrestrial basalt, and that

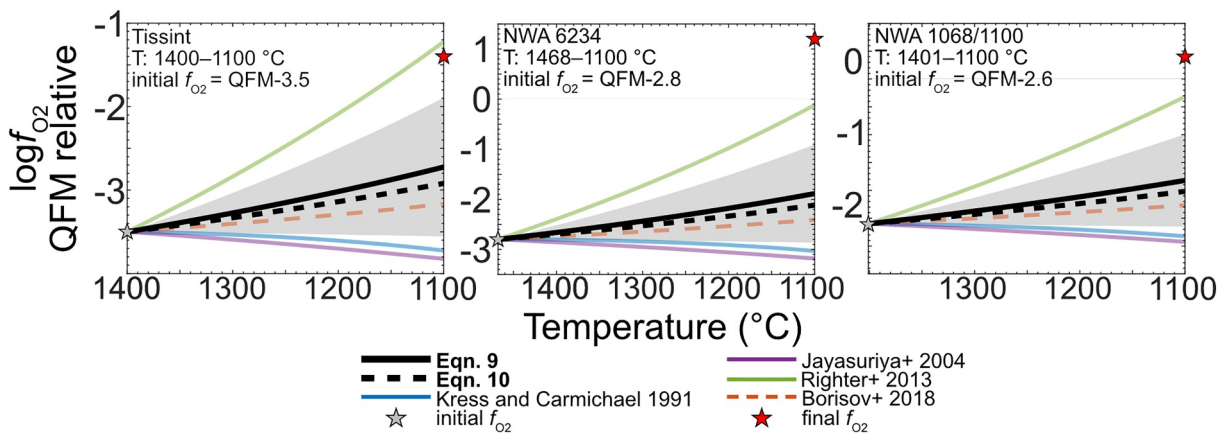

Figure 12. Comparison of predicted f_{O2} changes during unbuffered, isochemical cooling of shergottite liquids Tissint (Castle & Herd, 2017), NWA 6234 (Gross et al., 2013), and NWA 1068/1100 (Herd, 2006) from their liquids (1400°, 1468°, and 1401°C, respectively as determined by Rhyolite-MELTS) to 1100°C as calculated by different models. Horizontal temperature axis is reversed to portray cooling from left to right. Gray and red stars indicate f_{O2}s as recorded by shergottites at early and late stages of crystallization, respectively. Both martian-specific models, Equations 9 and 10, predict small amounts of oxidation during cooling at constant Fe^{3+}/Fe^{T}, indicating that additional processes (crysallization, decompression, assimilation, and/or degassing) are required to account for the observed oxidation evolution associated with martian magmatic evolution. Shaded area represents the 95% confidence intervals for the f_{O2} evolution predicted by Equation 9, calculated from 2-σ uncertainties for the regressed h-coefficient.

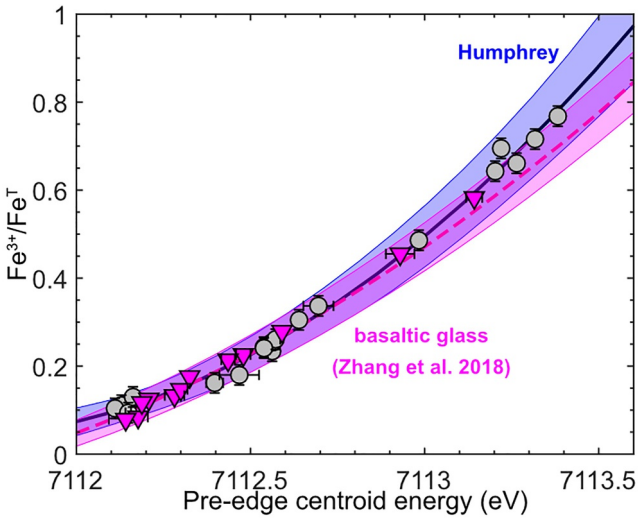

Figure 13. Comparison of Fe^{3+}/Fe^{T} versus XANES pre-edge centroid energies, including the calibrations and associated 95% confidence intervals for Humphrey glass (this study), and basaltic glasses defined by Zhang et al. (2018) and derived from glasses synthesized by Cottrell et al. (2009). Symbols follow Figure 7.

magma cooling already plays a significant role prior to the added influence of crystallization and other processes that modify melt Fe^{3+}/Fe^{T}.

4.8. A Non-Destructive Microbeam Technique to Measure Fe^{3+}/Fe^{T} in Martian Glasses

The development of microbeam XANES techniques to measure Fe^{3+}/Fe^{T} in micron-scale geological glasses, both experimental (Berry et al., 2003, 2018; Cottrell et al., 2009, 2018; Righter et al., 2013; Saper et al., 2024; Wilke et al., 2001, 2005; Zhang et al., 2016, 2017, 2018) and natural (Brounce et al., 2014, 2015, 2017; Cottrell & Kelley, 2011; Kelley & Cottrell, 2012; Moussallam, Longpré, et al., 2019; Moussallam, Oppenheimer, & Scaillet, 2019), improved characterization of magmatic redox by enabling non-destructive analysis with textural context and without requiring relatively large, homogenous glass samples. The application of XANES on natural and synthetic martian basalts has been implemented to broadly quantify f_{O_2} in crystalline martian materials (e.g., Bell et al., 2014; Nakada et al., 2020; Satake et al., 2014), application to Fe^{3+}/Fe^{T} in martian basaltic glasses has been limited to studies by McCanta et al. (2004) and Righter et al. (2013). However, the XANES technique presented in McCanta et al. (2004), calibrated on crystalline reference materials, is less precise than calibrations from geologic glass-reference materials (Berry et al., 2003; Botcharnikov et al., 2005; Cottrell et al., 2009; Wilke et al., 2005). Furthermore, the XANES technique presented by Righter et al. (2013) cannot be employed on martian glasses outside their study as centroid energies measured in that study are not standardized to a reference glass. Here, we present an updated martian-specific pre-edge centroid energy-Fe^{3+}/Fe^{T} calibration that incorporates the measurements and uncertainties from Mössbauer and XANES analyses of the Humphrey series. This calibration is applicable to analytical unknowns when the XANES centroid energies of a given analysis can be calibrated against the LW_0 reference glass (i.e., Cottrell et al., 2009), for which the centroid is taken as 7112.3 eV.

4.8.1. XANES Calibration

The Fe^{3+}/Fe^{T} versus XANES pre-edge centroid energy is fit as a weighted-least-squares polynomial quadratic function. The regression yields

$$\frac{Fe^{3+}}{Fe^{T}} = 0.0972 + 0.2388x + 0.2346x^2, \quad (12)$$

where x is the drift-corrected centroid energy minus 7112.111 eV (Figure 13).

We adopt the approach from Zhang et al. (2018) to calculate calibration uncertainties arising from instrumental uncertainties of Mössbauer and XANES spectroscopy, as well as the uncertainty of the recoil-free factor correction from Roskosz et al. (2022) by Monte-Carlo analysis (Zhang et al., 2018—Equation 9). 500-synthetic data sets are used to generate a variance-covariance matrix accounting for these uncertainties, which are then used to calculate calibration uncertainty (Data set S2). We use this calculation assuming a conservative estimate of XANES centroid uncertainty (±0.05 eV) to calculate 95% confidence intervals (Figure 13). For centroid energies 7112.118, 7112.299, and 7112.438, corresponding to Fe^{3+}/Fe^{T} ratios of 0.100, 0.150, and 0.200, the 1-σ Fe^{3+}/Fe^{T} uncertainties are ±0.014, 0.016, and 0.019. Notably, the calibration curves and associated 95% confidence intervals for Humphrey and basaltic glasses defined by Zhang et al. (2018) agree across much of the range of Fe^{3+}/Fe^{T} and centroid energies investigated. This suggests that XANES calibrations for terrestrial and basaltic glass compositions may yield results within error and that pre-edge centroid energy is a robust enough proxy for the Fe^{3+}/Fe^{T} ratio in basalt compositions despite the specific differences between martian and terrestrial basalts. The agreement between the curves is less close for more oxidized glasses, where the two trends diverge.

4.8.2. Application of XANES Calibration to Characterize Fe^{3+}/Fe^{T} in Partially Crystallized Experimental Glass

When applied to experiments relevant to martian magmatism, the XANES parameterization can be used to further constrain Fe-redox systematics at sub-liquidus temperatures and variable pressures. For example, experiment VF271 is the lowest temperature (1250°C) experiment synthesized and produced a subliquidus mixture of glass and crystals. Therefore, characterization of the Fe^{3+}/Fe^{T} ratio in the quenched glass requires microbeam analysis. Repeated XANES measurements of glassy portions of VF271 yield a corrected pre-edge centroid energy of 7113.425 ± 0.008 eV which corresponds to Fe^{3+}/Fe^{T} = 0.816 ± 0.022 or 0.727 ± 0.005, respectively, based on Equation 12 or (Zhang et al., 2018). Despite the congruence of Equation 12 and Zhang et al. (2018) calibration curves, the resolved Fe^{3+}/Fe^{T} ratios differ for oxidized glasses. Because the curve for Equation 12 is directly applicable to martian magmas, the accepted Fe^{3+}/Fe^{T} ratio of the VF271 glass is 0.816 ± 0.022.

Application of the XANES calibration (Equation 12) to quantify experimental martian glass Fe^{3+}/Fe^{T} at variable temperature and pressure, especially in partially crystallized assemblages not amenable for bulk Fe^{3+}/Fe^{T} characterization techniques, will expand the compositional, temperature, and pressure ranges of experiments which can be used to calibrate melt $Fe^{3+}/Fe^{T} - f_{O2}$ relationships. Furthermore, XANES characterization of melt Fe^{3+}/Fe^{T} in equilibrium with minerals can be leveraged to elucidate Fe^{3+} mineral-melt partitioning to better constrain iron redox systematics during partial melting of the martian magma and crystallization of the martian magma ocean (Matzen et al., 2022; Righter et al., 2013; Schaefer et al., 2024).

5. Conclusions

Martian basalt glasses with a composition similar to the parental liquid of Humphrey were synthesized at 100 kPa in a gas mixing furnace across a range of f_{O2}. Using Mössbauer spectroscopy and wet chemical colorimetry, we evaluated and further constrained the relationship between Fe^{3+}/Fe^{T}, f_{O2}, and temperature for high-FeO* martian basalt compositions and present two models (Equations 9 and 10) for the prediction of magmatic Fe^{3+}/Fe^{T} at a given f_{O2} and temperature. We find that the correlation between $\log\left(\frac{X_{Fe3+}}{X_{Fe2+}}\right)$ and $\log f_{O2}$ for martian magmas has a slope less than 0.25, with regressed values ranging from 0.19 to 0.22. The temperature dependence of $\log\left(\frac{X_{Fe3+}}{X_{Fe2+}}\right)$ is observed to be greater for martian magmas relative to previously investigated, non-martian silicate liquids.

Application of these models to depleted, intermediate, and enriched shergottite magmas (Tissint, NWA 6234, NWA 1068/1100) demonstrate that the extent of mass transfer required to explain multiple log units of f_{O2} increases terrestrial magma f_{O2}s less owing to the initially reduced nature of martian magmas (Figure 11). In addition, the increased sensitivity of $\log f_{O2}$ to changes in temperature provides evidence that the cooling of martian magmas leads to nearly 1 log unit of f_{O2} oxidation relative to QFM without requiring any increase in melt Fe^{3+}/Fe^{T} via crystallization or secondary processes that oxidize Fe^{2+} such as degassing or assimilation (Figure 12).

A martian-glass-specific XANES technique, calibrated from Mössbauer characterized experiments is also provided, allowing for non-destructive characterization of Fe^{3+}/Fe^{T} at micro-scale at high precision (±0.05). Application of this calibration is demonstrated in a partially crystallized experiment to validate its future application to other martian-relevant experiments containing micro-scale glass not previously amenable for Fe^{3+}/Fe^{T} characterization techniques.

Conflict of Interest

The authors declare no conflicts of interest relevant to this study.

Data Availability Statement

All data and code required for model parameterization and visualization are hosted in the Data Repository for U of M (DRUM) https://hdl.handle.net/11299/271200 (Aithala et al., 2025).

Acknowledgments
This work was supported by NASA Grant 80NSSC21K1826. The authors thank Maria Buss, Jasper Goldstein, Jed Mosenfelder, and Amanda Dillman for assistance with the lab work conducted for this study. SPA thanks Hongluo Zhang for assistance with Mössbauer fitting, Antonio Lanzirotti, Mathhew Newville, and Ryan Tappero for assistance with synchrotron-based XANES work, Liz Cottrell for loaning XANES basalt standard (NMNH 113716) and thoughtful discussions regarding XANES and magmatic redox, Peat Solheid for assisting with Mössbauer analyses, Jennifer Mitchell and Anette von der Handt for assistance with EPMA, and Jiaqi Li for assistance during wet chemical analyses.

References

Aithala, S. P., & Hirschmann, M. M. (2024). Evaluating the redox evolution of martian magmas. *Paper presented at 55th Lunar and Planetary Institute Science Conference, Abstract #2367*.

Aithala, S. P., Lange, R. A., & Hirschmann, M. M. (2025). Repository for: Controls on Iron-Redox State in Martian Magmas quantified by Mössbauer Spectroscopy, colorimetric wet chemistry, and XANES spectroscopy. Retrieved from the Data Repository for the University of Minnesota (DRUM) https://hdl.handle.net/11299/271200

Alberto, H. V., da Cunha, J. P., Mysen, B. O., Gil, J. M., & de Campos, N. A. (1996). Analysis of Mössbauer spectra of silicate glasses using a two-dimensional Gaussian distribution of hyperfine parameters. *Journal of Non-Crystalline Solids*, *194*(1–2), 48–57. https://doi.org/10.1016/0022-3093(95)00463-7

Bajt, S., Sutton, S. R., & Delaney, J. S. (1994). X-ray microprobe analysis of iron oxidation states in silicates and oxides using X-ray absorption near edge structure (XANES). *Geochimica et Cosmochimica Acta*, *58*(23), 5209–5214. https://doi.org/10.1016/0016-7037(94)90305-0

Ballhaus, C. (1993). Redox states of lithospheric and asthenospheric upper mantle. *Contributions to Mineralogy and Petrology*, *114*(3), 331–348. https://doi.org/10.1007/BF01046536

Balta, J. B., Sanborn, M., McSween, H. Y., & Wadhwa, M. (2013). Magmatic history and parental melt composition of olivine-phyric shergottite LAR 06319: Importance of magmatic degassing and olivine antecrysts in Martian magmatism. *Meteoritics & Planetary Science*, *48*(8), 1359–1382. https://doi.org/10.1111/maps.12140

Balta, J. B., Sanborn, M. E., Udry, A., Wadhwa, M., & McSween, H. Y. (2015). Petrology and trace element geochemistry of Tissint, the newest shergottite fall. *Meteoritics & Planetary Science*, *50*(1), 63–85. https://doi.org/10.1111/maps.12403

Barrat, J. A., Jambon, A., Bohn, M., Gillet, P. H., Sautter, V., Göpel, C., et al. (2002). Petrology and chemistry of the Picritic Shergottite North West Africa 1068 (NWA 1068). *Geochimica et Cosmochimica Acta*, *66*(19), 3505–3518. https://doi.org/10.1016/S0016-7037(02)00934-1

Bell, A. S., Burger, P. V., Le, L., Shearer, C. K., Papike, J. J., Sutton, S. R., et al. (2014). XANES measurements of Cr valence in olivine and their applications to planetary basalts. *American Mineralogist*, *99*(7), 1404–1412. https://doi.org/10.2138/am.2014.4646

Berry, A. J., St. O'Neill, H. C., Jayasuriya, K. D., Campbell, S. J., & Foran, G. J. (2003). XANES calibrations for the oxidation state of iron in a silicate glass. *American Mineralogist*, *88*(7), 967–977. https://doi.org/10.2138/am-2003-0704

Berry, A. J., Stewart, G. A., St. O'Neill, H. C., Mallmann, G., & Mosselmans, J. F. W. (2018). A re-assessment of the oxidation state of iron in MORB glasses. *Earth and Planetary Science Letters*, *483*, 114–123. https://doi.org/10.1016/j.epsl.2017.11.032

Bézos, A., Guivel, C., La, C., Fougeroux, T., & Humler, E. (2021). Unraveling the confusion over the iron oxidation state in MORB glasses. *Geochimica et Cosmochimica Acta*, *293*, 28–39. https://doi.org/10.1016/j.gca.2020.10.004

Bézos, A., & Humler, E. (2005). The Fe3+/ΣFe ratios of MORB glasses and their implications for mantle melting. *Geochimica et Cosmochimica Acta*, *69*(3), 711–725. https://doi.org/10.1016/j.gca.2004.07.026

Borisov, A., Behrens, H., & Holtz, F. (2013). The effect of titanium and phosphorus on ferric/ferrous ratio in silicate melts: An experimental study. *Contributions to Mineralogy and Petrology*, *166*(6), 1577–1591. https://doi.org/10.1007/s00410-013-0943-9

Borisov, A., Behrens, H., & Holtz, F. (2015). Effects of melt composition on Fe3+/Fe2+ in silicate melts: A step to model ferric/ferrous ratio in multicomponent systems. *Contributions to Mineralogy and Petrology*, *169*(2), 24. https://doi.org/10.1007/s00410-015-1119-6

Borisov, A., Behrens, H., & Holtz, F. (2017). Effects of strong network modifiers on Fe3+/Fe2+ in silicate melts: An experimental study. *Contributions to Mineralogy and Petrology*, *172*(5), 34. https://doi.org/10.1007/s00410-017-1337-1

Borisov, A., Behrens, H., & Holtz, F. (2018). Ferric/ferrous ratio in silicate melts: A new model for 1 atm data with special emphasis on the effects of melt composition. *Contributions to Mineralogy and Petrology*, *173*(12), 98. https://doi.org/10.1007/s00410-018-1524-8

Borisov, A., & McCammon, C. (2010). The effect of silica on ferric/ferrous ratio in silicate melts: An experimental study using Mossbauer spectroscopy. *American Mineralogist*, *95*(4), 545–555. https://doi.org/10.2138/am.2010.3217

Botcharnikov, R. E., Koepke, J., Holtz, F., McCammon, C., & Wilke, M. (2005). The effect of water activity on the oxidation and structural state of Fe in a ferro-basaltic melt. *Geochimica et Cosmochimica Acta*, *69*(21), 5071–5085. https://doi.org/10.1016/j.gca.2005.04.023

Bowman, W. S. (1995). Canadian diorite gneiss SY-4: Preparation and certification by eighty-nine international laboratories. *Geostandards Newsletter*, *19*(2), 101–124. https://doi.org/10.1111/j.1751-908x.1995.tb00156.x

Brounce, M., Boyce, J. W., & McCubbin, F. M. (2022). Sulfur in apatite from the Nakhla meteorite record a late-stage oxidation event. *Earth and Planetary Science Letters*, *595*, 117784. https://doi.org/10.1016/j.epsl.2022.117784

Brounce, M., Kelley, K. A., Cottrell, E., & Reagan, M. K. (2015). Temporal evolution of mantle wedge oxygen fugacity during subduction initiation. *Geology*, *43*(9), 775–778. https://doi.org/10.1130/G36742.1

Brounce, M., Stolper, E., & Eiler, J. (2017). Redox variations in Mauna Kea lavas, the oxygen fugacity of the Hawaiian plume, and the role of volcanic gases in Earth's oxygenation. *Proceedings of the National Academy of Sciences*, *114*(34), 8997–9002. https://doi.org/10.1073/pnas.1619527114

Brounce, M. N., Kelley, K. A., & Cottrell, E. (2014). Variations in Fe3+/∑Fe of Mariana Arc Basalts and Mantle wedge fO2. *Journal of Petrology*, *55*(12), 2513–2536. https://doi.org/10.1093/petrology/egu065

Canil, D. (1997). Vanadium partitioning and the oxidation state of Archaean komatiite magmas. *Nature*, *389*(6653), 842–845. https://doi.org/10.1038/39860

Carmichael, I. S. E. (1991). The redox states of basic and silicic magmas: A reflection of their source regions? *Contributions to Mineralogy and Petrology*, *106*(2), 129–141. https://doi.org/10.1007/BF00306429

Castle, N., & Herd, C. D. K. (2017). Experimental petrology of the Tissint meteorite: Redox estimates, crystallization curves, and evaluation of petrogenetic models. *Meteoritics & Planetary Science*, *52*(1), 125–146. https://doi.org/10.1111/maps.12739

Christie, D. M., Carmichael, I. S. E., & Langmuir, C. H. (1986). Oxidation states of mid-ocean ridge basalt glasses. *Earth and Planetary Science Letters*, *79*(3–4), 397–411. https://doi.org/10.1016/0012-821X(86)90195-0

Corrigan, G., & Gibb, F. G. F. (1979). The loss of Fe and Na from a basaltic melt during experiments using the wire-loop method. *Mineralogical Magazine*, *43*(325), 121–126. https://doi.org/10.1180/minmag.1979.043.325.10

Cottrell, E., Birner, S. K., Brounce, M., Davis, F. A., Waters, L. E., & Kelley, K. A. (2021). Oxygen fugacity across tectonic settings. In R. Moretti & D. R. Neuville (Eds.), *Geophysical monograph series* (1st ed., pp. 33–61). Wiley. https://doi.org/10.1002/9781119473206.ch3

Cottrell, E., & Kelley, K. A. (2011). The oxidation state of Fe in MORB glasses and the oxygen fugacity of the upper mantle. *Earth and Planetary Science Letters*, *305*(3–4), 270–282. https://doi.org/10.1016/j.epsl.2011.03.014

Cottrell, E., Kelley, K. A., Lanzirotti, A., & Fischer, R. A. (2009). High-precision determination of iron oxidation state in silicate glasses using XANES. *Chemical Geology*, *268*(3–4), 167–179. https://doi.org/10.1016/j.chemgeo.2009.08.008

Cottrell, E., Lanzirotti, A., Mysen, B., Birner, S., Kelley, K. A., Botcharnikov, R., et al. (2018). A Mössbauer-based XANES calibration for hydrous basalt glasses reveals radiation-induced oxidation of Fe. *American Mineralogist*, *103*(4), 489–501. https://doi.org/10.2138/am-2018-6268

Dasgupta, R. (2013). Ingassing, storage, and outgassing of terrestrial carbon through geologic time. *Reviews in Mineralogy and Geochemistry*, *75*(1), 183–229. https://doi.org/10.2138/rmg.2013.75.7

Dasgupta, R., & Hirschmann, M. M. (2010). The deep carbon cycle and melting in Earth's interior. *Earth and Planetary Science Letters*, *298*(1–2), 1–13. https://doi.org/10.1016/j.epsl.2010.06.039

De Grave, E., & Van Alboom, A. (1991). Evaluation of ferrous and ferric Mössbauer fractions. *Physics and Chemistry of Minerals*, *18*(5), 337–342. https://doi.org/10.1007/bf00200191

Ding, S., Dasgupta, R., & Tsuno, K. (2014). Sulfur concentration of martian basalts at sulfide saturation at high pressures and temperatures–implications for deep sulfur cycle on Mars. *Geochimica et Cosmochimica Acta*, *131*, 227–246. https://doi.org/10.1016/j.gca.2014.02.003

Dingwell, D. B. (1991). Redox viscometry of some Fe-bearing silicate melts. *American Mineralogist*, *76*, 1560–1562.

Donovan, J. J., & Tingle, T. (1996). An improved mean atomic number background correction for quantitative microanalysis. *Journal of Microscopy and Microanalysis*, *2*, 1–7. https://doi.org/10.1017/s1431927696210013

Dyar, M. D., Agresti, D. G., Schaefer, M. W., Grant, C. A., & Sklute, E. C. (2006). Mössbauer spectroscopy of earth and planetary materials. *Annual Review of Earth and Planetary Sciences*, *34*(1), 83–125. https://doi.org/10.1146/annurev.earth.34.031405.125049

Dyar, M. D., McCanta, M., Lanzirotti, A., Steven, C. J., & Ytsma, C. (2023). Calibration for iron redox state and oxygen fugacity in silicate glasses from x-ray absorption spectroscopy. *Chemical Geology*, *635*, 121605. https://doi.org/10.1016/j.chemgeo.2023.121605

Eugster, H. P. (1957). Heterogeneous reactions involving oxidation and reduction at high pressures and temperatures. *The Journal of Chemical Physics*, *26*(6), 1760–1761. https://doi.org/10.1063/1.1743626

Ferdous, J., Brandon, A. D., Peslier, A. H., & Pirotte, Z. (2017). Evaluating crustal contributions to enriched shergottites from the petrology, trace elements, and Rb-Sr and Sm-Nd isotope systematics of Northwest Africa 856. *Geochimica et Cosmochimica Acta*, *211*, 280–306. https://doi.org/10.1016/j.gca.2017.05.032

Filiberto, J. (2017). Geochemistry of Martian basalts with constraints on magma genesis. *Chemical Geology*, *466*, 1–14. https://doi.org/10.1016/j.chemgeo.2017.06.009

Flanagan, F. J., & Kirschenbaum, H. (1984). The precision of classical rock analysis. *Geostandards Newsletter*, *8*(1), 7–11. https://doi.org/10.1111/j.1751-908X.1984.tb00403.x

Fudali, R. F. (1965). Oxygen fugacities of basaltic and andesitic magmas. *Geochimica et Cosmochimica Acta*, *29*(9), 1063–1075. https://doi.org/10.1016/0016-7037(65)90103-1

Ghiorso, M. S., & Evans, B. W. (2008). Thermodynamics of rhombohedral oxide solid solutions and a revision of the FE-TI two-oxide geothermometer and oxygen-barometer. *American Journal of Science*, *308*(9), 957–1039. https://doi.org/10.2475/09.2008.01

Goodrich, C. A., Herd, C. D. K., & Taylor, L. A. (2003). Spinels and oxygen fugacity in olivine-phyric and lherzolitic shergottites. *Meteoritics & Planetary Science*, *38*(12), 1773–1792. https://doi.org/10.1111/j.1945-5100.2003.tb00014.x

Gross, J., Filiberto, J., Herd, C. D. K., Daswani, M. M., Schwenzer, S. P., & Treiman, A. H. (2013). Petrography, mineral chemistry, and crystallization history of olivine-phyric shergottite NWA 6234: A new melt composition. *Meteoritics & Planetary Science*, *48*(5), 854–871. https://doi.org/10.1111/maps.12092

Gualda, G. A. R., & Ghiorso, M. S. (2015). MELTS_Excel: A microsoft excel-based MELTS interface for research and teaching of magma properties and evolution. *Geochemistry, Geophysics, Geosystems*, *16*, 315–324. https://doi.org/10.1002/2014GC005545

Gualda, G. A. R., Ghiorso, M. S., Lemons, R. V., & Carley, T. L. (2012). Rhyolite-MELTS: A modified calibration of MELTS optimized for Silica-rich, fluid-bearing magmatic systems. *Journal of Petrology*, *53*(5), 875–890. https://doi.org/10.1093/petrology/egr080

Helz, R. T., Cottrell, E., Brounce, M. N., & Kelley, K. A. (2017). Olivine-melt relationships and syneruptive redox variations in the 1959 eruption of Kīlauea Volcano as revealed by XANES. *Journal of Volcanology and Geothermal Research*, *333–334*, 1–14. https://doi.org/10.1016/j.jvolgeores.2016.12.006

Herd, C. D. K. (2003). The oxygen fugacity of olivine-phyric martian basalts and the components within the mantle and crust of Mars. *Meteoritics & Planetary Science*, *38*(12), 1793–1805. https://doi.org/10.1111/j.1945-5100.2003.tb00015.x

Herd, C. D. K. (2006). Insights into the redox history of the NWA 1068/1110 martian basalt from mineral equilibria and vanadium oxybarometry. *American Mineralogist*, *91*(10), 1616–1627. https://doi.org/10.2138/am.2006.2104

Herd, C. D. K. (2019). Reconciling redox: Making spatial and temporal sense of oxygen fugacity variations in martian igneous rocks. *Paper presented at 50th Lunar and Planetary Institute Science Conference, Abstract #2746*.

Herd, C. D. K., Borg, L. E., Jones, J. H., & Papike, J. J. (2002). Oxygen fugacity and geochemical variations in the martian basalts: Implications for martian basalt petrogenesis and the oxidation state of the upper mantle of Mars. *Geochimica et Cosmochimica Acta*, *66*(11), 2025–2036. https://doi.org/10.1016/S0016-7037(02)00828-1

Herd, C. D. K., Papike, J. J., & Brearley, A. J. (2001). Oxygen fugacity of martian basalts from electron microprobe oxygen and TEM-EELS analyses of Fe-Ti oxides. *American Mineralogist*, *86*(9), 1015–1024. https://doi.org/10.2138/am-2001-8-908

Hirschmann, M. M. (2012). Magma ocean influence on early atmosphere mass and composition. *Earth and Planetary Science Letters*, *341–344*, 48–57. https://doi.org/10.1016/j.epsl.2012.06.015

Hirschmann, M. M. (2022). Magma oceans, iron and chromium redox, and the origin of comparatively oxidized planetary mantles. *Geochimica et Cosmochimica Acta*, *328*, 221–241. https://doi.org/10.1016/j.gca.2022.04.005

Holland, H. D. (2002). Volcanic gases, black smokers, and the great oxidation event. *Geochimica et Cosmochimica Acta*, *66*(21), 3811–3826. https://doi.org/10.1016/S0016-7037(02)00950-X

Holloway, J. R., & Jakobsson, S. (1986). Volatile solubilities in magmas: Transport of volatiles from mantles to planet surfaces. *Journal of Geophysical Research*, *91*(B4), 505–508. https://doi.org/10.1029/JB091iB04p0D505

Howarth, G. H., Pernet-Fisher, J. F., Balta, J. B., Barry, P. H., Bodnar, R. J., & Taylor, L. A. (2014). Two-stage polybaric formation of the new enriched, pyroxene-oikocrystic, lherzolitic shergottite, NWA 7397. *Meteoritics & Planetary Science*, *49*(10), 1812–1830. https://doi.org/10.1111/maps.12357

Howarth, G. H., & Udry, A. (2017). Trace elements in olivine and the petrogenesis of the intermediate, olivine-phyric shergottite NWA 10170. *Meteoritics & Planetary Science*, *52*(2), 391–409. https://doi.org/10.1111/maps.12799

Huebner, J. S., & Sato, M. (1970). The oxygen fugacity-temperature relationships of manganese oxide and nickel oxide buffers. *American Mineralogist: Journal of Earth and Planetary Materials*, *55*(5–6), 934–952.

Jayasuriya, K. D., St. O'Neill, H. C., Berry, A. J., & Campbell, S. J. (2004). A Mössbauer study of the oxidation state of Fe in silicate melts. *American Mineralogist*, *89*(11–12), 1597–1609. https://doi.org/10.2138/am-2004-11-1203

Jiang, Y., & Hsu, W. (2012). Petrogenesis of Grove Mountains 020090: An enriched "lherzolitic" shergottite. *Meteoritics & Planetary Science*, *47*(9), 1419–1435. https://doi.org/10.1111/j.1945-5100.2012.01404.x

Jochum, K. P., Stoll, B., Herwig, K., Willbold, M., Hofmann, A. W., Amini, M., et al. (2006). MPI-DING reference glasses for in situ micro-analysis: New reference values for element concentrations and isotope ratios. *Geochemistry, Geophysics, Geosystems*, *7*(2). https://doi.org/10.1029/2005gc001060

Kasting, J. F. (1993). Earth's early atmosphere. *Science*, *259*(5097), 920–926. https://doi.org/10.1126/science.11536547

Kelley, K. A., & Cottrell, E. (2012). The influence of magmatic differentiation on the oxidation state of Fe in a basaltic arc magma. *Earth and Planetary Science Letters*, *329–330*, 109–121. https://doi.org/10.1016/j.epsl.2012.02.010

Kennedy, G. C. (1948). Equilibrium between volatiles and iron oxides in igneous rocks. *American Journal of Science*, *246*(9), 529–548. https://doi.org/10.2475/ajs.246.9.529

Kilinc, A., Carmichael, I. S. E., Rivers, M. L., & Sack, R. O. (1983). The ferric-ferrous ratio of natural silicate liquids equilibrated in air. *Contributions to Mineralogy and Petrology*, *83*(1–2), 136–140. https://doi.org/10.1007/BF00373086

Kress, V. C., & Carmichael, I. S. E. (1988). Stoichiometry of the iron oxidation reaction in silicate melts. *American Mineralogist*, *73*(11–12), 1267–1274.

Kress, V. C., & Carmichael, I. S. E. (1991). The compressibility of silicate liquids containing Fe_2O_3 and the effect of composition, temperature, oxygen fugacity and pressure on their redox states. *Contributions to Mineralogy and Petrology*, *108*(1–2), 82–92. https://doi.org/10.1007/BF00307328

Lagarec, K., & Rancourt, D. G. (1997). Extended Voigt-based analytic lineshape method for determining N-dimensional correlated hyperfine parameter distributions in Mössbauer spectroscopy. *Nuclear Instruments and Methods in Physics Research Section B: Beam Interactions with Materials and Atoms*, *129*(2), 266–280. https://doi.org/10.1016/S0168-583X(97)00284-X

Lange, R., & Carmichael, I. S. E. (1989). Ferric-ferrous equilibria in Na20-FeO-Fe203 -Si02 melts: Effects of analytical techniques on derived partial molar volumes. *Geochimica et Cosmochimica Acta*, *53*(9), 2195–2204. https://doi.org/10.1016/0016-7037(89)90343-8

Lin, Y., Guan, Y., Wang, D., Kimura, M., & Leshin, L. A. (2005). Petrogenesis of the new lherzolitic shergottite Grove Mountains 99027: Constraints of petrography, mineral chemistry, and rare Earth elements. *Meteoritics & Planetary Science*, *40*(11), 1599–1619. https://doi.org/10.1111/j.1945-5100.2005.tb00134.x

Lodders, K. (1998). A survey of shergottite, nakhlite and chassigny meteorites whole-rock compositions. *Meteoritics & Planetary Science*, *33*(S4). https://doi.org/10.1111/j.1945-5100.1998.tb01331.x

Marinenko, R. B. (1982). *Preparation and characterization 0F K-411 and K-412 mineral glasses* (Vol. 260, p. 74). National Bureau of Standards Special Publication.

Matzen, A. K., Woodland, A., Beckett, J. R., & Wood, B. J. (2022). Oxidation state of iron and Fe-Mg partitioning between olivine and basaltic martian melts. *American Mineralogist*, *107*(7), 1442–1452. https://doi.org/10.2138/am-2021-7682

McCanta, M. C., Dyar, M. D., Rutherford, M. J., & Delaney, J. S. (2004). Iron partitioning between basaltic melts and clinopyroxene as a function of oxygen fugacity. *American Mineralogist*, *89*(11–12), 1685–1693. https://doi.org/10.2138/am-2004-11-1214

McCubbin, F. M., Elardo, S. M., Shearer, C. K., Smirnov, A., Hauri, E. H., & Draper, D. S. (2013). A petrogenetic model for the comagmatic origin of chassignites and nakhlites: Inferences from chlorine-rich minerals, petrology, and geochemistry. *Meteoritics & Planetary Science*, *48*(5), 819–853. https://doi.org/10.1111/maps.12095

McSween, H. Y., Wyatt, M. B., Gellert, R., Bell, J. F. III., Morris, R. V., Herkenhoff, K. E., et al. (2006). Characterization and petrologic interpretation of olivine-rich basalts at Gusev Crater, Mars. *Journal of Geophysical Research*, *111*(E2), E02S10. https://doi.org/10.1029/2005JE002477

Morris, R. V., Golden, D. C., Bell, J. F., & Lauer, H. V. (1995). Hematite, pyroxene, and phyllosilicates on Mars: Implications from oxidized impact melt rocks from Manicouagan Crater, Quebec, Canada. *Journal of Geophysical Research*, *100*(E3), 5319–5328. https://doi.org/10.1029/94JE01500

Morris, R. V., Klingelhöfer, G., Schröder, C., Rodionov, D. S., Yen, A., Ming, D. W., et al. (2006). Mössbauer mineralogy of rock, soil, and dust at Gusev crater, Mars: Spirit's journey through weakly altered olivine basalt on the plains and pervasively altered basalt in the Columbia Hills. *Journal of Geophysical Research*, *111*(E2), 2005JE002584. https://doi.org/10.1029/2005JE002584

Moussallam, Y., Longpré, M. A., McCammon, C., Gomez-Ulla, A., Rose-Koga, E. F., Scaillet, B., et al. (2019). Mantle plumes are oxidised. *Earth and Planetary Science Letters*, *527*, 115798. https://doi.org/10.1016/j.epsl.2019.115798

Moussallam, Y., Oppenheimer, C., & Scaillet, B. (2019). On the relationship between oxidation state and temperature of volcanic gas emissions. *Earth and Planetary Science Letters*, *520*, 260–267. https://doi.org/10.1016/j.epsl.2019.05.036

Moussallam, Y., Oppenheimer, C., Scaillet, B., Gaillard, F., Kyle, P., Peters, N., et al. (2014). Tracking the changing oxidation state of Erebus magmas, from mantle to surface, driven by magma ascent and degassing. *Earth and Planetary Science Letters*, *393*, 200–209. https://doi.org/10.1016/j.epsl.2014.02.055

Mukhopadhyay, B., Basu, S., & Holdaway, M. J. (1993). A discussion of Margules-type formulations for multicomponent solutions with a generalized approach. *Geochimica et Cosmochimica Acta*, *57*(2), 277–283. https://doi.org/10.1016/0016-7037(93)90430-5

Mysen, B. O., Carmichael, I. S. E., & Virgo, D. (1985). A comparison of iron redox ratios in silicate glasses determined by wet-chemical and ^{57}Fe Mössbauer resonant absorption methods. *Contributions to Mineralogy and Petrology*, *90*(2–3), 101–106. https://doi.org/10.1007/BF00378253

Nakada, R., Usui, T., Ushioda, M., & Takahashi, Y. (2020). Vanadium micro-XANES determination of oxygen fugacity in olivine-hosted glass inclusion and groundmass glasses of martian primitive shergottite Yamato 980459. *American Mineralogist*, *105*(11), 1695–1703. https://doi.org/10.2138/am-2020-7321

Newville, M. (2013). Larch: An analysis package for XAFS and related spectroscopies. *Journal of Physics: Conference Series*, *430*, 012007. https://doi.org/10.1088/1742-6596/430/1/012007

Nicklas, R. W., Day, J. M. D., Vaci, Z., Udry, A., Liu, Y., & Tait, K. T. (2021). Uniform oxygen fugacity of shergottite mantle sources and an oxidized martian lithosphere. *Earth and Planetary Science Letters*, *564*, 116876. https://doi.org/10.1016/j.epsl.2021.116876

St. O'Neill, H. C. (1987). Quartz–fayalite–iron and quartz–fayalite–magnetite equilibria and the free-energy of formation of fayalite (Fe2SiO4) and magnetite (Fe3O4). *American Mineralogist*, *72*, 67–75.

O'Neill, H. S. C., & Pownceby, M. I. (1993). Thermodynamic data from redox reactions at high temperatures. I. An experimental and theoretical assessment of the electrochemical method using stabilized zirconia electrolytes, with revised values for the Fe-"FeO", Co-CoO, Ni-NiO and Cu-Cu2O oxygen buffers, and new data for the W-WO2 buffer. *Contributions to Mineralogy and Petrology*, *114*(3), 296–314. https://doi.org/10.1007/bf01046533

Ostwald, A., Udry, A., Payré, V., Gazel, E., & Wu, P. (2022). The role of assimilation and fractional crystallization in the evolution of the Mars crust. *Earth and Planetary Science Letters*, *585*, 117514. https://doi.org/10.1016/j.epsl.2022.117514

Ottonello, G., Moretti, R., Marini, L., & Vetuschi Zuccolini, M. (2001). Oxidation state of iron in silicate glasses and melts: A thermochemical model. *Chemical Geology*, *174*(1–3), 157–179. https://doi.org/10.1016/S0009-2541(00)00314-4

Pahlevan, K., Schaefer, L., & Hirschmann, M. M. (2019). Hydrogen isotopic evidence for early oxidation of silicate Earth. *Earth and Planetary Science Letters*, *526*, 115770. https://doi.org/10.1016/j.epsl.2019.115770

Partzsch, G. M., Lattard, D., & McCammon, C. (2004). Mössbauer spectroscopic determination of Fe3+/Fe2+ in synthetic basaltic glass: A test of empirical fO2 equations under superliquidus and subliquidus conditions. *Contributions to Mineralogy and Petrology*, *147*(5), 565–580. https://doi.org/10.1007/s00410-004-0571-5

Peslier, A. H., Hnatyshin, D., Herd, C. D. K., Walton, E. L., Brandon, A. D., Lapen, T. J., & Shafer, J. T. (2010). Crystallization, melt inclusion, and redox history of a Martian meteorite: Olivine-phyric shergottite Larkman Nunatak 06319. *Geochimica et Cosmochimica Acta*, *74*(15), 4543–4576. https://doi.org/10.1016/j.gca.2010.05.002

Potts, P. J., Thompson, M., & Wilson, S. (2002). G-Probe-1-An international proficiency Test for Microprobe Laboratories-Report on round 1: February 2002 (TB-1 basaltic glass). *Geostandards Newsletter*, *26*(2), 197–235. https://doi.org/10.1111/j.1751-908x.2002.tb00887.x

Righter, K., Danielson, L. R., Pando, K., Morris, R. V., Graff, T. G., Agresti, D. G., et al. (2013). Redox systematics of martian magmas with implications for magnetite stability. *American Mineralogist*, *98*(4), 616–628. https://doi.org/10.2138/am.2013.4251

Righter, K., Keller, L. P., Rahman, Z., & Christoffersen, R. (2014). Redox-driven exsolution of iron-titanium oxides in magnetite in Miller Range (MIL) 03346 nakhlite: Evidence for post crystallization oxidation in the nakhlite cumulate pile? *American Mineralogist*, *99*(11–12), 2313–2319. https://doi.org/10.2138/am-2014-4926

Rohrbach, A., & Schmidt, M. W. (2011). Redox freezing and melting in the Earth's deep mantle resulting from carbon–iron redox coupling. *Nature*, *472*(7342), 209–212. https://doi.org/10.1038/nature09899

Roskosz, M., Dauphas, N., Hu, J., Hu, M. Y., Neuville, D. R., Brown, D., et al. (2022). Structural, redox and isotopic behaviors of iron in geological silicate glasses: A NRIXS study of Lamb-Mössbauer factors and force constants. *Geochimica et Cosmochimica Acta*, *321*, 184–205. https://doi.org/10.1016/j.gca.2022.01.021

Rubin, A. E., Warren, P. H., Greenwood, J. P., Verish, R. S., Box, P. O., Leshin, L. A., et al. (2000). Los Angeles: The most differentiated basaltic martian meteorite. *Geology*, *28*(11), 1011–1014. https://doi.org/10.1130/0091-7613(2000)28<1011:LATMDB>2.0.CO;2

Sack, R. O., Carmichael, I. S. E., Rivers, M., & Ghiorso, M. S. (1981). Ferric-ferrous equilibria in natural silicate liquids at 1 bar. *Contributions to Mineralogy and Petrology*, *75*(4), 369–376. https://doi.org/10.1007/BF00374720

Sack, R. O., & Ghiorso, M. S. (1989). Importance of considerations of mixing properties in establishing an internally consistent thermodynamic database: Thermochemistry of minerals in the system Mg2SiO4-Fe2SiO4-SiO2. *Contributions to Mineralogy and Petrology*, *102*(1), 41–68. https://doi.org/10.1007/BF01160190

Sack, R. O., & Ghiorso, M. S. (1994a). Thermodynamics of multicomponent pyroxenes: I. Formulation of a general model. *Contributions to Mineralogy and Petrology*, *116*(3), 277–286. https://doi.org/10.1007/BF00306497

Sack, R. O., & Ghiorso, M. S. (1994b). Thermodynamics of multicomponent pyroxenes: II. Phase relations in the quadrilateral. *Contributions to Mineralogy and Petrology*, *116*(3), 287–300. https://doi.org/10.1007/BF00306498

Sack, R. O., & Ghiorso, M. S. (1994c). Thermodynamics of multicomponent pyroxenes: III. Calibration of Fe2+(Mg)_-1, TiAI2(MgSi2)_-1, $TiFe_2^{3+}$ (MgSi2)_-1, AIFe3+(MgSi)_-1, NaAI(CaMg}_-1, AI2(MgSi}_-1 and Ca(Mg}_-1 exchange reactions between pyroxenes and silicate melts. *Contributions to Mineralogy and Petrology*, *118*(3), 271–296. https://doi.org/10.1007/BF00306648

Saper, L. M., Baker, M. B., Brounce, M., Hughes, E. C., Hofmann, A. E., & Stolper, E. M. (2024). Experimental constraints on iron and sulfur redox equilibria and kinetics in basaltic melt inclusions. *Geochimica et Cosmochimica Acta*, *381*, 75–96. https://doi.org/10.1016/j.gca.2024.07.018

Satake, W., Mikouchi, T., & Miyamoto, M. (2014). Redox states of thirteen shergottites as inferred from iron micro X-ray absorption near edge structure of maskelynite. *Geochemical Journal*, *48*(1), 85–98. https://doi.org/10.2343/geochemj.2.0288

Schaefer, L., Pahlevan, K., & Elkins-Tanton, L. T. (2024). Ferric iron evolution during crystallization of the Earth and Mars. *Journal of Geophysical Research: Planets*, *129*(9), e2023JE008262. https://doi.org/10.1029/2023JE008262

Schmidt, M. E., Schrader, C. M., & McCoy, T. J. (2013). The primary fO2 of basalts examined by the Spirit rover in Gusev Crater, Mars: Evidence for multiple redox states in the martian interior. *Earth and Planetary Science Letters*, *384*, 198–208. https://doi.org/10.1016/j.epsl.2013.10.005

Shearer, C. K., Aaron, P. M., Burger, P. V., Guan, Y., Bell, A. S., & Papike, J. J. (2013). Petrogenetic linkages among fO_2, isotopic enrichments-depletions and crystallization history in Martian basalts. Evidence from the distribution of phosphorus in olivine megacrysts. *Geochimica et Cosmochimica Acta*, *120*, 17–38. https://doi.org/10.1016/j.gca.2013.06.034

Stagno, V., Ojwang, D. O., McCammon, C. A., & Frost, D. J. (2013). The oxidation state of the mantle and the extraction of carbon from Earth's interior. *Nature*, *493*(7430), 84–88. https://doi.org/10.1038/nature11679

Symes, S. J. K., Borg, L. E., Shearer, C. K., & Irving, A. J. (2008). The age of the martian meteorite Northwest Africa 1195 and the differentiation history of the shergottites. *Geochimica et Cosmochimica Acta*, *72*(6), 1696–1710. https://doi.org/10.1016/j.gca.2007.12.022

The MathWorks Inc. (2020). *MATLAB version: 9.9.0 (R2020b)*. The MathWorks Inc. Retrieved from https://www.mathworks.com

Thornber, C. R., Roeder, P. L., & Foster, J. R. (1980). The effect of composition on the ferric-ferrous ratio in basaltic liquids at atmospheric pressure. *Geochimica et Cosmochimica Acta*, *44*(3), 525–532. https://doi.org/10.1016/0016-7037(80)90048-4

Trail, D., Watson, E. B., & Tailby, N. D. (2011). The oxidation state of Hadean magmas and implications for early Earth's atmosphere. *Nature*, *480*(7375), 79–82. https://doi.org/10.1038/nature10655

Tsuchiyama, A., Nagahara, H., & Kushiro, I. (1981). Volatilization of sodium from silicate melt spheres and its application to the formation of chondrules. *Geochimica et Cosmochimica Acta*, *45*(8), 1357–1367. https://doi.org/10.1016/0016-7037(81)90228-3

Udry, A., Howarth, G. H., Herd, C. D. K., Day, J. M. D., Lapen, T. J., & Filiberto, J. (2020). What Martian meteorites reveal about the interior and surface of Mars. *Journal of Geophysical Research: Planets*, *125*(12), e2020JE006523. https://doi.org/10.1029/2020JE006523

Usui, T., McSween, H. Y., & Floss, C. (2008). Petrogenesis of olivine-phyric shergottite Yamato 980459, revisited. *Geochimica et Cosmochimica Acta*, *72*(6), 1711–1730. https://doi.org/10.1016/j.gca.2008.01.011

Wadhwa, M., Lentz, R. C. F., McSWEEN, H. Y., & Crozaz, G. (2001). A petrologic and trace element study of Dar al Gani 476 and Dar al Gani 489: Twin meteorites with affinities to basaltic and lherzolitic shergottites. *Meteoritics & Planetary Science*, *36*(2), 195–208. https://doi.org/10.1111/j.1945-5100.2001.tb01864.x

Walton, E. L., Irving, A. J., Bunch, T. E., & Herd, C. D. K. (2012). Northwest Africa 4797: A strongly shocked ultramafic poikilitic shergottite related to compositionally intermediate Martian meteorites. *Meteoritics & Planetary Science*, *47*(9), 1449–1474. https://doi.org/10.1111/j.1945-5100.2012.01407.x

Wang, Z., Tian, W., & Di, Y. (2021). New temperature and oxygen fugacity data of Martian nakhlite from Northwest Africa (NWA) 5790 and implications for shallow sulphur degassing. *Earth Planets and Space*, *73*(1), 164. https://doi.org/10.1186/s40623-021-01492-3

White, W. M., & Klein, E. M. (2014). Composition of the Oceanic crust. In *Treatise on geochemistry* (pp. 457–496). Elsevier. https://doi.org/10.1016/B978-0-08-095975-7.00315-6

Wilke, M., Farges, F., Petit, P.-E., Brown, G. E., & Martin, F. (2001). Oxidation state and coordination of Fe in minerals: An Fe *K*- XANES spectroscopic study. *American Mineralogist*, *86*(5–6), 714–730. https://doi.org/10.2138/am-2001-5-612

Wilke, M., Partzsch, G. M., Bernhardt, R., & Lattard, D. (2005). Determination of the iron oxidation state in basaltic glasses using XANES at the K-edge. *Chemical Geology*, *220*(1–2), 143–161. https://doi.org/10.1016/j.chemgeo.2005.03.004

Wilson, A. D. (1960). The micro-determination of ferrous iron in silicate minerals by a volumetric and a colorimetric method. *The Analyst*, *85*(1016), 823. https://doi.org/10.1039/an9608500823

Wood, B. J. (1990). An experimental test of the spinel peridotite oxygen barometer. *Journal of Geophysical Research*, *95*(B10), 15845–15851. https://doi.org/10.1029/JB095iB10p15845

York, D. (1968). Least squares fitting of a straight line with correlated errors. *Earth and Planetary Science Letters*, *5*, 320–324. https://doi.org/10.1016/S0012-821X(68)80059-7

Zhang, H. L. (2022). Advances of ferrous and ferric Mössbauer recoilless fractions in minerals and glasses. *Geoscience Frontiers*, *13*(2), 101316. https://doi.org/10.1016/j.gsf.2021.101316

Zhang, H. L., Cottrell, E., Solheid, P. A., Kelley, K. A., & Hirschmann, M. M. (2018). Determination of Fe3+/ΣFe of XANES basaltic glass standards by Mössbauer spectroscopy and its application to the oxidation state of iron in MORB. *Chemical Geology*, *479*, 166–175. https://doi.org/10.1016/j.chemgeo.2018.01.006

Zhang, H. L., Hirschmann, M. M., Cottrell, E., Newville, M., & Lanzirotti, A. (2016). Structural environment of iron and accurate determination of Fe3+/ΣFe ratios in andesitic glasses by XANES and Mössbauer spectroscopy. *Chemical Geology*, *428*, 48–58. https://doi.org/10.1016/j.chemgeo.2016.02.022

Zhang, H. L., Hirschmann, M. M., Cottrell, E., & Withers, A. C. (2017). Effect of pressure on Fe3+/ΣFe ratio in a mafic magma and consequences for magma ocean redox gradients. *Geochimica et Cosmochimica Acta*, *204*, 83–103. https://doi.org/10.1016/j.gca.2017.01.023

Zhang, H. L., Solheid, P. A., Lange, R. A., Von Der Handt, A., & Hirschmann, M. M. (2015). Accurate determination of $Fe^{3+}/\sum Fe$ of andesitic glass by Mössbauer spectroscopy. *American Mineralogist*, *100*(8–9), 1967–1977. https://doi.org/10.2138/am-2015-5161

Zipfel, J., Scherer, P., Spettel, B., Dreibus, G., & Schultz, L. (2000). Petrology and chemistry of the new shergottite Dar al Gani 476. *Meteoritics & Planetary Science*, *35*(1), 95–106. https://doi.org/10.1111/j.1945-5100.2000.tb01977.x